JFM PAPERS

Heat transfer in drop-laden turbulence

Francesca Mangani[1]**, Alessio Roccon**[1,2]**, Francesco Zonta**[1] **and Alfredo Soldati**[1,2],†

[1]Institute of Fluid Mechanics and Heat Transfer, TU-Wien, 1060 Vienna, Austria

[2]Polytechnic Department of Engineering and Architecture, University of Udine, 33100 Udine, Italy

Heat transfer by large deformable drops in a turbulent flow is a complex and rich-in-physics system, in which drop deformation, breakage and coalescence influence the transport of heat. We study this problem by coupling direct numerical simulation (DNS) of turbulence with a phase-field method for the interface description. Simulations are run at fixed-shear Reynolds and Weber numbers. To evaluate the influence of microscopic flow properties, like momentum/thermal diffusivity, on macroscopic flow properties, like mean temperature or heat transfer rates, we consider four different values of the Prandtl number, which is the momentum to thermal diffusivity ratio: $Pr = 1$, $Pr = 2$, $Pr = 4$ and $Pr = 8$. The drop volume fraction is $\Phi \simeq 5.4\,\%$ for all cases. Drops are initially warmer than the turbulent carrier fluid and release heat at different rates depending on the value of Pr, but also on their size and on their own dynamics (topology, breakage, drop–drop interaction). Computing the time behaviour of the drops and carrier fluid average temperatures, we clearly show that an increase of Pr slows down the heat transfer process. We explain our results by a simplified phenomenological model: we show that the time behaviour of the drop average temperature is self-similar, and a universal behaviour can be found upon rescaling by $t/Pr^{2/3}$. Accordingly, the heat transfer coefficient $\mathcal{H}$ (respectively its dimensionless counterpart, the Nusselt number Nu) scales as $\mathcal{H} \sim Pr^{-2/3}$ (respectively $Nu \sim Pr^{1/3}$) at the beginning of the simulation, and tends to $\mathcal{H} \sim Pr^{-1/2}$ (respectively $Nu \sim Pr^{1/2}$) at later times. These different scalings can be explained via the boundary layer theory and are consistent with previous theoretical/numerical predictions.

Key words: turbulence simulation, drops, breakup/coalescence

† Email address for correspondence: alfredo.soldati@tuwien.ac.at

1. Introduction

Transport of passive and active scalars in multiphase turbulence is very important in many industrial processes and natural phenomena, from vaporization of atomized fuel jets (Gorokhovski & Herrmann 2008; Ashgriz 2011; Gao *et al.* 2022; Boyd & Ling 2023) to rain formation and atmosphere–ocean heat/mass exchanges (Duguid & Stampfer 1971; Deike 2022) or even to the uptake of nutrients and other biochemicals by cells in complex flows (Aksnes & Egge 1991; Magar & Pedley 2005). While the mixing of active or passive scalars in turbulent single-phase flows has been extensively analysed using experiments and simulations (Kim & Moin 1989; Kasagi, Tomita & Kuroda 1992; Antonia & Orlandi 2003; Pirozzoli, Bernardini & Orlandi 2016; Zonta, Marchioli & Soldati 2012*a*; Zonta, Onorato & Soldati 2012*b*; Zonta & Soldati 2014), when multiphase flows are considered, the situation becomes much more challenging (Gauding *et al.* 2022; Ni 2024).

One crucial aspect of multiphase turbulence – which makes the analysis of these flows particularly difficult – is the presence of interfaces that dynamically move and deform in time and space according to the flow conditions and that clearly alter/mediate heat and species transport and mixing, as well as phase change phenomena (Deckwer 1980; Gvozdić *et al.* 2018; Liu *et al.* 2022; Pelusi *et al.* 2023; Roccon, Zonta & Soldati 2023).

In this context, previous works mostly focused on the heat/mass transfer from/to isolated drops and bubbles using analytical (Boussinesq 1905; Levich 1962; Bird, Stewart & Lightfoot 2002), numerical (Bothe *et al.* 2004; Figueroa-Espinoza & Legendre 2010; Herlina & Wissink 2016; Albernaz *et al.* 2017; Farsoiya, Popinet & Deike 2021; Farsoiya *et al.* 2023) and experimental techniques (Ohta, Shimoyama & Ohigashi 1975; Hiromitsu & Kawaguchi 1995; Wu *et al.* 2003; Birouk & Gökalp 2006; Marti *et al.* 2017). When swarms of drops/bubbles are considered, the number of available investigations is more limited. For very small drops/bubbles, numerical investigations usually rely on the Lagrangian approach, in which drops/bubbles are assumed to have sub-Kolmogorov size and are treated as material points (Kuerten 2016; Maxey 2017; Chong *et al.* 2021; Wang *et al.* 2021*a*; Wang, Dalla Barba & Picano 2021*b*). When larger drops/bubbles are considered (i.e. larger than the Kolmogorov scale), the problem becomes more complex, since the interface shape and deformation play a crucial role. Not surprisingly, remarkable works in this context have appeared only recently, both for the case of passive scalar transport and for the case of active scalars/phase change (Méès *et al.* 2020; Dodd *et al.* 2021; Scapin *et al.* 2022; Shao, Jin & Luo 2022; Hidman *et al.* 2023). Relevant to the present work is the observation done by Dodd *et al.* (2021) and Scapin *et al.* (2022), and also confirmed by the experiments of Méès *et al.* (2020), where the Sherwood number (i.e. dimensionless mass transfer coefficient) measured during drop evaporation in turbulence is larger compared to that obtained from widely used correlations (Frössling 1938; Ranz 1952; Birouk & Gökalp 2002).

In this work, we focus on the numerical simulation of the heat transfer process in a drop-laden turbulent channel flow, particularly on the role of the Prandtl number *Pr*, i.e. the ratio between momentum and thermal diffusivity, in the process. Compared with single-phase turbulence, where the range of scales that must be resolved to perform a direct numerical simulation (DNS) is purely dictated by the smallest scales of turbulence (Kolmogorov scale), when the mixing of scalars in multiphase turbulence is analysed, two further additional scales come into the picture. The first one is the Batchelor scale (Batchelor 1959; Batchelor, Howells & Townsend 1959), which determines the smallest scale of the temperature/concentration field. The second important scale is the Kolmogorov–Hinze scale (Kolmogorov 1941; Hinze 1955), and is linked to the multiphase nature of the flow. This scale can be used, perhaps with some limitations (Qi *et al.* 2022),

to determine the critical size of a drop/bubble that will not undergo breakage in turbulence. These two scales – and their corresponding ratio to the Kolmogorov scale, i.e. the smallest length scale of the turbulent flow field – control the system dynamics and define the minimal grid requirements that must be satisfied to perform a DNS of scalar mixing in multiphase turbulence (always keeping in mind that performing a simulation that resolves the interface dynamics down to the molecular scale is, at present, almost unfeasible). In this context, the major constraint is usually posed by the Batchelor scale, which becomes smaller than the Kolmogorov length scale when Prandtl numbers larger than unity are considered. Overall, the wide range of scales involved in the process makes simulations of scalar mixing in multiphase turbulence a challenging task and limits the space parameters that can be explored by means of DNS. Our simulations are initialized by injecting a swarm of large and deformable drops (initially warmer) inside a turbulent channel flow (initially colder). The system is described by coupling the DNS of turbulent heat transfer with a phase-field method, employed to describe the drop topology (Zheng *et al.* 2015; Mirjalili, Jain & Mani 2022). We simulate realistic values of the Prandtl number up to $Pr = 8$, similar to those obtained in liquid–liquid systems. We remark here that simulations of mass transfer problems in wall-bounded flow configurations, where the typical Schmidt number Sc (i.e. the mass transfer counterpart of Pr) is $O(10^2 \sim 10^3)$, e.g. $Sc \simeq 600$ for CO_2 in freshwater (Wanninkhof 1992), are currently out of reach even using the most advanced computing. Indeed, the resulting Batchelor scale would be at least one order of magnitude smaller, thus requiring grid resolutions comparable to or larger than those employed for state-of-the-art single-phase DNS (Lee & Moser 2015; Pirozzoli *et al.* 2021) but with a much larger computational cost as the systems of equations to be solved are more complex and restrictive (also from the temporal discretization point of view).

The present study has three main objectives. First, we want to investigate the macroscopic dynamic of the drops and of the heat transfer process by analysing the drop size distribution and the mean temperature behaviour of the two phases over time. Second, we want to characterize the influence of the Prandtl number, i.e. of the microscopic flow properties, on the macroscopic flow properties (mean temperature, heat transfer coefficient) and, building on top of the numerical results, we want to develop a physical-based model to explain the observed results. Third, we want to study the influence of the Prandtl number and drop size on the temperature distribution inside the drops, so as to evaluate the corresponding flow mixing/ homogenization.

The paper is organized as follows. In § 2, the governing equations, the numerical method and the simulation setup are presented. In § 3, the simulation results, in terms of drop size distribution and mean temperature of the two phases and heat transfer coefficient, are carefully characterized and discussed. A simplified model is also developed to explain the observed results. The temperature distribution inside the drops is then evaluated at different Prandtl numbers and drop sizes. Finally, conclusions are presented in § 4.

2. Methodology

We consider a swarm of large and deformable drops injected in a turbulent channel flow. The channel has dimensions $L_x \times L_y \times L_z = 4\pi h \times 2\pi h \times 2h$ along the streamwise (x), spanwise (y) and wall-normal direction (z). To describe the dynamics of the system, we couple DNS of the Navier–Stokes and energy equations, used to describe the turbulent flow, with a phase-field method (PFM), used to describe the interfacial phenomena. The employed numerical framework is described in more detail in the following.

2.1. *Phase-field method*

To describe the dynamics of drops and the corresponding topological changes (e.g. coalescence and breakage), we employ an energy-based PFM (Jacqmin 1999; Badalassi, Ceniceros & Banerjee 2003; Roccon *et al.* 2023), which is based on the introduction of a scalar quantity, the phase field ϕ, required to identify the two phases. The phase field ϕ has a uniform value in the bulk of each phase ($\phi = +1$ inside the drops; $\phi = -1$ inside the carrier fluid) and undergoes a smooth change across the thin transition layer that separates the two phases. The transport of the phase field variable is described by a Cahn–Hilliard equation, which in dimensionless form reads as

$$\frac{\partial \phi}{\partial t} + \boldsymbol{u} \cdot \boldsymbol{\nabla} \phi = \frac{1}{Pe} \nabla^2 \mu_\phi + f_p, \qquad (2.1)$$

where $\boldsymbol{u} = (u, v, w)$ is the velocity vector, Pe is the Péclet number, μ is the phase field chemical potential and f_p is a penalty-flux term which will be further discussed later. The Péclet number is

$$Pe = \frac{u_\tau^* h^*}{\mathcal{M}^* \beta^*}, \qquad (2.2)$$

where u_τ^* is the friction velocity ($u_\tau^* = \sqrt{\tau_w^*/\rho^*}$, with τ_w^* the wall-shear stress and $\rho^* = \rho_c^* = \rho_d^*$ the density of the fluids), h^* is the channel half-height, $\mathcal{M}^*$ is the mobility and β^* is a positive constant (the superscript * is used to denote dimensional quantities hereinafter). The chemical potential μ is defined as the variational derivative of a Ginzburg–Landau free-energy functional, the expression of which is chosen to represent an immiscible binary mixture of fluids (Soligo, Roccon & Soldati 2019*a*,*b*,*c*). The functional is the sum of two contributions: the first contribution, f_0, accounts for the tendency of the system to separate into the two pure stable phases, while the second contribution, f_{mix}, is a mixing term accounting for the energy stored at the interface (i.e. surface tension). The mathematical expression of the functional in dimensionless form is

$$\mathcal{F}[\phi, \boldsymbol{\nabla}\phi] = \int_\Omega \left(\underbrace{\frac{(\phi^2 - 1)^2}{4}}_{f_0} + \underbrace{\frac{Ch^2}{2}|\boldsymbol{\nabla}\phi|^2}_{f_{mix}} \right) \mathrm{d}\Omega, \qquad (2.3)$$

where Ω is the considered domain and Ch is the Cahn number, which represents the dimensionless thickness of the thin interfacial layer between the two fluids:

$$Ch = \frac{\xi^*}{h^*}, \qquad (2.4)$$

where ξ^* is clearly the dimensional thickness of the interfacial layer. From (2.3), the expression of the chemical potential can be derived as the functional derivative with respect to the order parameter:

$$\mu_\phi = \frac{\delta \mathcal{F}[\phi \boldsymbol{\nabla}\phi]}{\delta \phi} = \phi^3 - \phi - Ch^2 \nabla^2 \phi. \qquad (2.5)$$

At equilibrium, the chemical potential is constant throughout all the domain. The equilibrium profile for a flat interface can thus be obtained by solving $\boldsymbol{\nabla} \mu_\phi = \boldsymbol{0}$, hence,

$$\phi_{eq} = \tanh\left(\frac{s}{\sqrt{2}Ch}\right), \qquad (2.6)$$

where s is the coordinate normal to the interface. As anticipated before, the last term in the right-hand side of the Cahn–Hilliard equation (2.1) is a penalty-flux term employed

in the profile-corrected formulation of the PFM, and is used to overcome some potential drawbacks of the standard formulation of the method, e.g. mass leakages among the phases and misrepresentation of the interfacial profile (Yue, Zhou & Feng 2007; Li, Choi & Kim 2016). This penalty flux is defined as

$$f_p = \frac{\lambda}{Pe}\left[\nabla^2\phi - \frac{1}{\sqrt{2}Ch}\nabla\cdot\left((1-\phi^2)\frac{\nabla\phi}{|\nabla\phi|}\right)\right], \tag{2.7}$$

where $\lambda = 0.0625/Ch$ (Soligo *et al.* 2019c).

2.2. *Hydrodynamics*

To describe the hydrodynamics of the multiphase system, the Cahn–Hilliard equation is coupled with the Navier–Stokes equations. The presence of a deformable interface (and of the corresponding surface tension forces) is accounted for by introducing an interfacial term in the Navier–Stokes equations. Recalling that in the present case, we consider two fluids with the same density ($\rho^* = \rho_c^* = \rho_d^*$) and viscosity ($\mu^* = \mu_c^* = \mu_d^*$), the continuity and Navier–Stokes equations in dimensionless form read as

$$\nabla\cdot\boldsymbol{u} = 0, \tag{2.8}$$

$$\frac{\partial\boldsymbol{u}}{\partial t} + \boldsymbol{u}\cdot\nabla\boldsymbol{u} = -\nabla p + \frac{1}{Re_\tau}\nabla^2\boldsymbol{u} + \frac{3}{\sqrt{8}}\frac{Ch}{We}\nabla\cdot\boldsymbol{T_c}. \tag{2.9}$$

Here p is the pressure field, while $\boldsymbol{T_c}$ is the Korteweg tensor (Korteweg 1901) used to account for the surface tension forces and defined as

$$\boldsymbol{T_c} = |\nabla\phi|^2\boldsymbol{I} - \nabla\phi\otimes\nabla\phi, \tag{2.10}$$

where $\boldsymbol{I}$ is the identity matrix and $\otimes$ represents the dyadic product. This approach is the continuum surface stress approach (Lafaurie *et al.* 1994; Gueyffier *et al.* 1999) applied in the context of the PFM, and is analytically equivalent to the chemical potential forcing (Mirjalili, Khanwale & Mani 2023). The dimensionless groups appearing in the Navier–Stokes equations are the shear Reynolds number Re_τ (ratio between inertial and viscous forces) and the Weber number We (ratio between inertial and surface tension forces), which are defined as

$$Re_\tau = \frac{\rho^* u_\tau^* h^*}{\mu^*}, \quad We = \frac{\rho^* u_\tau^{*2} h^*}{\sigma^*}, \tag{2.11a,b}$$

where σ^* is the surface tension. Note that, consistently with the employed adimensionalization, We is defined using the half-channel height (and not the drop diameter).

2.3. *Energy equation*

The time evolution of the temperature field is obtained by solving the energy equation using a one-scalar model approach (Zheng *et al.* 2015). To avoid the introduction of further complexity in the system, we consider two fluids with the same thermophysical properties, i.e. same thermal conductivity λ^*, same specific heat capacity c_p^* and therefore same thermal diffusivity $a^* = \lambda^*/\rho^* c_p^*$ (since the density of the two phases is also the same). These properties have been evaluated at a reference temperature $\theta_r^* = (\theta_{d,0}^* + \theta_{c,0}^*)/2$,

i.e. the average between the initial drop temperature and the carrier fluid temperature, and are assumed to be constant and uniform. Within these assumptions, the energy equation written in dimensionless form reads as

$$\frac{\partial \theta}{\partial t} + \boldsymbol{u} \cdot \boldsymbol{\nabla} \theta = \frac{1}{Re_\tau Pr} \nabla^2 \theta, \tag{2.12}$$

where Pr is the Prandtl number defined as

$$Pr = \frac{\mu^* c_p^*}{\lambda^*} = \frac{\nu^*}{a^*}, \tag{2.13}$$

with $\nu^* = \mu^*/\rho^*$ the kinematic viscosity (i.e. momentum diffusivity). From a physical viewpoint, Pr represents the momentum-to-thermal diffusivity ratio.

2.4. *Numerical discretization*

The governing equations (2.1), (2.8), (2.9) and (2.12) are solved using a pseudo-spectral method, which uses Fourier series along the periodic directions (streamwise and spanwise) and Chebyshev polynomials along the wall-normal direction. The Navier–Stokes and continuity equations are solved using a wall-normal velocity-vorticity formulation: (2.9) is rewritten as a fourth-order equation for the wall-normal component of the velocity *w* and a second-order equation for the wall-normal component of the vorticity ω_z (Kim, Moin & Moser 1987; Speziale 1987). The Cahn–Hilliard equation (2.1), which in its original form is a fourth-order equation and is split into two second-order equations using the splitting scheme proposed by Badalassi *et al.* (2003). Using this scheme, the governing equations are recast as a coupled system of Helmholtz equations, which can be readily solved.

The governing equations are time-advanced using an implicit-explicit scheme. For the Navier–Stokes, the linear part is integrated using a Crank–Nicolson implicit scheme, while the nonlinear part is integrated using an Adams–Bashforth explicit scheme. Similarly, for the Cahn–Hilliard and energy equations, the linear terms are integrated using an implicit Euler scheme, while the nonlinear terms are integrated in time using an Adams–Bashforth scheme. The adoption of the implicit Euler scheme for the Cahn–Hilliard equation helps to damp unphysical high-frequency oscillations that could arise from the steep gradients of the phase field.

As the characteristic length scales of the flow and temperature fields, represented by the Kolmogorov scale, η_k^+, and the Batchelor scale, η_θ^+, are different when non-unitary Prandtl numbers are employed (being these two quantities linked by the following relation $\eta_\theta^+ = \eta_k^+/\sqrt{Pr}$), a dual grid approach is employed to reduce the computational cost of the simulations and, at the same time, to fulfil the DNS requirements. In particular, when super-unitary Prandtl numbers are simulated, a finer grid is used to resolve the energy equation. Spectral interpolation is used to upscale/downscale the fields from the coarse to the refined grid and *vice versa* when required (e.g. upscaling of the velocity field to compute the advection terms in the energy equation).

This numerical scheme has been implemented in a parallel Fortran 2003 MPI in-house proprietary code. The parallelization strategy is based on a 2-D domain decomposition to divide the workload among all the MPI tasks. The solver execution is accelerated using openACC directives and CUDA Fortran instructions (solver execution) while the Nvidia cuFFT libraries are used to accelerate the execution of the Fourier/Chebyshev transforms. Overall, the computational method adopted allows for the accurate resolution of all the governing equations and the achievement of an excellent parallel efficiency

thanks to the fine-grain parallelism offered by the numerical method used. The equivalent computational cost of the simulations is approximately 25 million CPU hours and the resulting dataset has a size of approximately 16 TB.

2.5. *Boundary conditions*

The system of governing equations is complemented by a set of suitable boundary conditions. For the Navier–Stokes equations, no-slip boundary conditions are enforced at the top and bottom walls (located at $z = \pm h$):

$$\boldsymbol{u}(z = \pm h) = \boldsymbol{0}. \tag{2.14}$$

For the Cahn–Hilliard equation, no-flux boundary conditions are applied at the two walls, yielding to the following boundary conditions:

$$\frac{\partial \phi}{\partial z}(z = \pm h) = 0; \quad \frac{\partial^3 \phi}{\partial z^3}(z = \pm h) = 0. \tag{2.15a,b}$$

Likewise, for the energy equation, no-flux boundary conditions are applied at the two walls (i.e. adiabatic walls):

$$\frac{\partial \theta}{\partial z}(z = \pm h) = 0. \tag{2.16}$$

Along the streamwise and spanwise directions (x and y), periodic boundary conditions are imposed for all variables (Fourier discretization). The adoption of these boundary conditions leads to the conservation of the phase field and temperature fields over time:

$$\frac{\partial}{\partial t} \int_{\Omega} \phi \, d\Omega = 0; \quad \frac{\partial}{\partial t} \int_{\Omega} \theta \, d\Omega = 0, \tag{2.17a,b}$$

where Ω is the computational domain. Regarding the phase-field, (2.17*a,b*) enforces mass conservation of the entire system but does not guarantee the conservation of the mass of each phase (Yue *et al.* 2007; Soligo *et al.* 2019*c*), as some leakages between the phases may occur. This drawback is rooted in the PFM and more specifically in the curvature-driven flux produced by the chemical potential gradients (Kwakkel, Fernandino & Dorao 2020; Mirjalili & Mani 2021). This issue is successfully mitigated with the adoption of the profile-corrected formulation that largely reduces this phenomenon. In the present cases, mass leakage between the phases occurs only in the initial transient when the phase field is initialized (see the section below for details on the initial condition) and is limited to 2 % of the initial mass of the drops. After this initial transient, the mass of each phase remains constant.

2.6. *Simulation set-up*

The turbulent channel flow, driven by an imposed constant pressure gradient in the streamwise direction, has a shear Reynolds number $Re_\tau = 300$. The computational domain has dimensions $L_x \times L_y \times L_z = 4\pi h \times 2\pi h \times 2h$, which corresponds to $L_x^+ \times L_y^+ \times L_z^+ = 3770 \times 1885 \times 600$ wall units. The value of the Weber number is kept constant and is equal to $We = 3.00$, so to be representative of liquid/liquid mixtures (Than *et al.* 1988). To study the influence of the Prandtl number Pr on the heat transfer process, we consider four different values of Pr: $Pr = 1$, $Pr = 2$, $Pr = 4$ and $Pr = 8$. These values cover a wide range of real-case scenarios: from low-Prandtl-number fluids to water–toluene mixtures.

Case	Re_τ	We	Pr	$N_x \times N_y \times N_z$ (NS+CH)	$N_x \times N_y \times N_z$ (Energy)
Single phase	300	—	—	$512 \times 256 \times 257$	—
Drop laden	300	3.0	1.0	$1024 \times 512 \times 513$	$1024 \times 512 \times 513$
Drop laden	300	3.0	2.0	$1024 \times 512 \times 513$	$1024 \times 512 \times 513$
Drop laden	300	3.0	4.0	$1024 \times 512 \times 513$	$2048 \times 1024 \times 1025$
Drop laden	300	3.0	8.0	$1024 \times 512 \times 513$	$2048 \times 1024 \times 1025$

Table 1. Overview of the simulation parameters. For a fixed shear Reynolds number $Re_\tau = 300$ and Weber number $We = 3$, we consider a single-phase flow case and four non-isothermal drop-laden flows characterized by different Prandtl numbers: from $Pr = 1$ to $Pr = 8$. The grid resolution is modified accordingly so as to satisfy DNS requirements.

The grid resolution used to resolve the continuity, Navier–Stokes and Cahn–Hilliard equations is equal to $N_x \times N_y \times N_z = 1024 \times 512 \times 513$ for all the cases considered in this work. For the energy equation, the same grid used for the flow field and phase field is employed at the lower Prandtl numbers ($Pr = 1$ and $Pr = 2$), while a more refined grid, with $N_x \times N_y \times N_z = 2048 \times 1024 \times 513$ points, is used when the larger Prandtl numbers are considered ($Pr = 4$ and $Pr = 8$). The computational grid has uniform spacing in the homogeneous directions, while Chebyshev–Gauss–Lobatto points are used in the wall-normal direction. We refer the reader to table 1 for an overview of the main physical and computational parameters of the simulation. For the employed grid resolution, the Cahn number is set to $Ch = 0.01$ while, to achieve convergence to the sharp interface limit, the corresponding phase field Péclet number is $Pe = 1/Ch = 50$.

All simulations are initialized by releasing a regular array of 256 spherical drops with diameter $d = 0.4h$ (corresponding to $d^+ = 120w.u.$) inside a fully developed turbulent flow field (obtained from a preliminary simulation). To ensure the independence of the results from the initial flow field condition, each case is initialized with a slightly different flow field realization. Naturally, the fields are equivalent in terms of statistics as they are all obtained from a statistically steady turbulent channel flow. The volume fraction of the drops is $\Phi = V_d/(V_c + V_d) = 5.4\%$, with V_d and V_c the volume of the drops and carrier fluid, respectively.

The initial condition for the temperature field is such that all drops are initially warm (initial temperature $\theta_{d,0} = 1$), while the carrier fluid is initially cold (initial temperature $\theta_{c,0} = 0$). To avoid numerical instabilities that might arise from a discontinuous temperature field, the transition between drops and carrier fluid is initially smoothed using a hyperbolic tangent kernel. Figure 1 (which is an instantaneous snapshot captured at $t^+ = 1000$, for $Pr = 1$) shows a volume rendering of the temperature field (blue, cold; red, hot), inside which deformable drops (whose interface, iso-level $\phi = 0$, is shown in white) are transported.

3. Results

Results obtained from the numerical simulations will be first discussed from a qualitative viewpoint, by looking at instantaneous flow and drop visualizations, and then analysed from a more quantitative viewpoint, by looking at the drop size distribution (DSD), and at the effect of the Prandtl number Pr on the average drops and fluid temperature. To explain the numerical results, and to offer a possible parametrization of the heat transfer process in drop-laden flows, we will also develop a simplified phenomenological model of the system. Finally, we will characterize the temperature distribution inside the drops, elucidating the
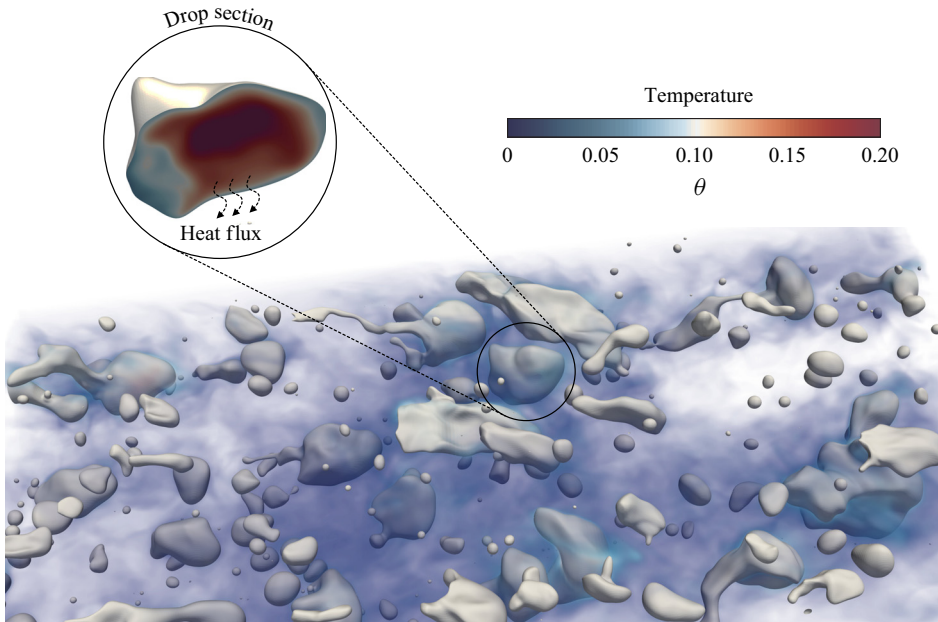
978 A12-8

Figure 1. Rendering of the computational setup employed for the simulations. A swarm of large and deformable drops is released in a turbulent channel flow. The temperature field is volume-rendered (blue, low; red, high) and the drop interface is shown in white (iso-level $\phi = 0$). Drops have a temperature higher than the carrier fluid (close-up view). The snapshot refers to $Pr = 1$ and $t^+ = 1000$.

effects of Pr and of the drop size on it. Note that, unless differently mentioned, results are presented using the wall-unit scaling system but for the temperature field, which is made dimensionless using the initial temperature difference as a reference scale (which is a natural choice in the present case).

3.1. *Qualitative discussion*

The complex dynamics of drops immersed in a non-isothermal turbulent flow is visualized in figure 1, where the drops (identified by iso-contour of $\phi = 0$) are shown together with a volume-rendered distribution of temperature in the carrier fluid. Also shown in figure 1 is a close-up view of the temperature distribution inside the drop. We can notice that most of the drops – because of their deformability – gather at the channel centre, as also observed in previous studies in similar configurations (Scarbolo, Bianco & Soldati 2016; Soligo, Roccon & Soldati 2020; Mangani *et al.* 2022).

Once injected into the flow, each drop starts interacting with the flow and with the neighbouring drops. The result of the drop–turbulence and drop–drop interactions is the occurrence of breakage and coalescence events. A breakage event happens when the flow vigorously stretches the drop, leading to the formation of a thin ligament that breaks and generates two child drops. Upon separation, surface tension forces tend to retract the broken filaments and restore the drop spherical shape. A coalescence event is observed when two drops come close to each other. The small liquid film that separates the drops starts to drain, and a coalescence bridge is formed. Later, surface tension forces enter the picture, reshaping the drop and completing the coalescence process. The dynamic competition between breakage and coalescence events, and their interaction
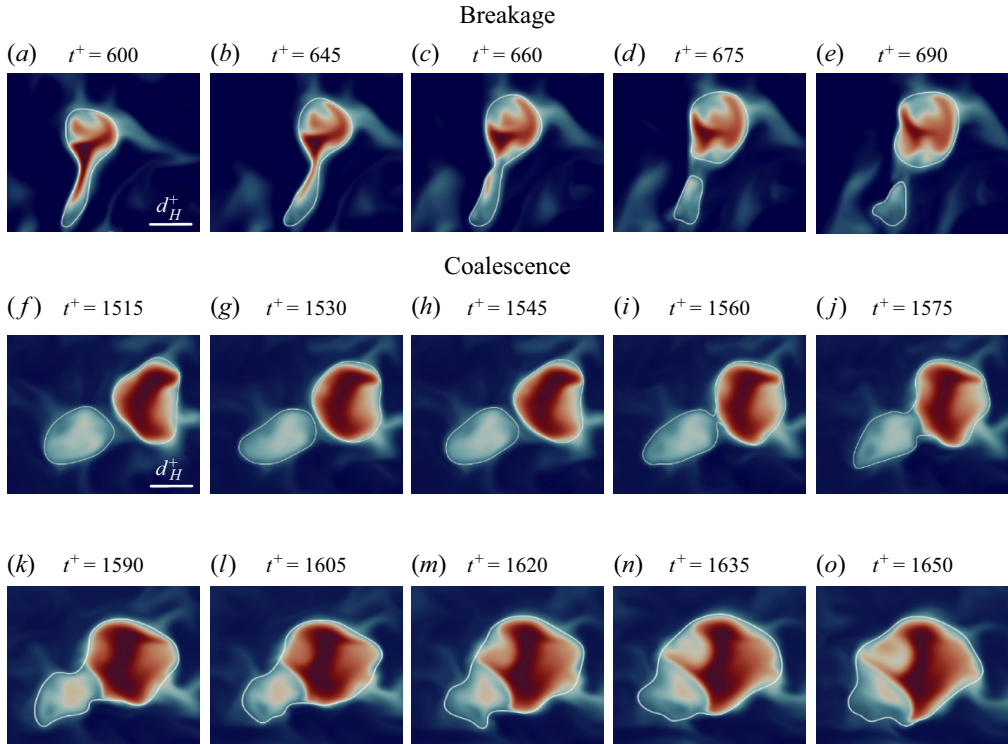
Breakage

Coalescence

Figure 2. Influence of topology changes on heat transfer: time sequence (a–e) of a breakage event and (f–o) of a coalescence event. During a breakage event, heat is transferred from the drops to carrier fluid thanks to the high surface/volume ratio of the pinch-off region. In the middle and bottom rows, the mixing between parcels of fluid with different temperatures can be appreciated. The two sequences refer to the case $Pr = 1$ and snapshots are separated by $\Delta t^+ = 15$. As a reference, the Kolmogorov–Hinze scale, d_H^+, is also reported.

with the turbulent flow, determines the number of drops, their size distribution, and their shape/morphology (i.e. curvature, interfacial area, etc.).

In the present case, drops not only exchange momentum with the flow and with the other drops but also heat. Starting from an initial condition characterized by warm drops (with uniform temperature) and cold carrier fluid, and because of the imposed adiabatic boundary conditions, the system evolves towards an equilibrium isothermal state. During the transient to attain this thermal equilibrium state, heat is transported by diffusion and advection inside each of the two phases, and across the interface of the drops (see the temperature field inside and outside the drops, figure 1). The picture is then further complicated by the occurrence of breakage and coalescence events. This is represented in figure 2. When breakage occurs (figure 2a–e), a thin filament is generated (figure 2a–c), which then leads to the formation of a smaller satellite drop (figure 2d,e). The filament and the satellite drop, given the large surface-to-volume ratio, exchange heat very efficiently and rapidly become colder. In contrast, when a coalescence occurs (figure 2f–o), two drops having different temperatures merge together. This induces an efficient mixing process, during which cold parcels of one drop become warmer and *vice versa*, warm parcels of the other drops become colder. Overall, breakup and coalescence events induce heat transfer modifications that are, in general, hard to predict *a priori*, since they do depend on the relative size of the involved parents/child drops.

978 A12-10

Naturally, the problem of heat transfer in drop-laden turbulence is strongly influenced by the Prandtl number of the flow. This can be appreciated by looking at figure 3, where we show the instantaneous temperature field, together with the shape of the drops, at a certain instant in time ($t^+ = 1500$) and at different Prandtl numbers: (*a*) $Pr = 1$; (*b*) $Pr = 2$; (*c*) $Pr = 4$ and (*d*) $Pr = 8$. In each panel, the temperature field is shown on a wall-parallel x^+-y^+ plane located at the channel centre ($z^+ = 0$) and is visualized with a blue-red scale (blue, low; red, high). We observe that the temperature field changes significantly with Pr. In particular, we notice an increase in the drop-to-fluid temperature difference for increasing Pr, going from $Pr = 1$ (figure 3*a*) where this difference is small, to $Pr = 8$ (figure 3*d*) where this difference is large. The heat transfer from the drops to the carrier fluid becomes slower as Pr increases, consistent with a physical situation in which the Pr number is increased by reducing the thermal diffusivity of the fluid while keeping the momentum diffusivity constant (i.e. constant kinematic viscosity, and hence shear Reynolds number). Also, the temperature structures, both inside and outside the drop, become thinner and more complicated at higher Pr, since their characteristic length scale, the Batchelor scale $\eta_\theta^+ \propto Pr^{-1/2}$, becomes smaller for increasing Pr (Batchelor 1959; Batchelor *et al.* 1959). In addition, smaller drops have, on average, a lower temperature compared to larger drops, regardless of the value of Pr. All these aspects will be discussed in more detail in the next sections.

3.2. *Drop size distribution*

To characterize the collective dynamics of the drops, we compute the DSD at steady-state conditions, averaging over a time window $\Delta t^+ = 3000$, from $t^+ = 3000$ to 6000. The achievement of steady-state conditions is here evaluated by monitoring global flow properties, like flow rate and wall stress, and drop properties, like the number of drops and the overall drop surface. It is worth mentioning that a quasi-equilibrium DSD, very close to the steady one, is already achieved at $t^+ \simeq 750$, and only minor changes occur to the DSD afterwards.

Figure 4 shows the DSD obtained for the different cases considered here: $Pr = 1$ (dark violet), $Pr = 2$ (violet), $Pr = 4$ (pink) and $Pr = 8$ (light pink). Drop size distribution profiles are statistically the same. Small differences are due to the initial turbulence field, which is different for each simulation (see § 2.6). The DSDs have been computed considering, for each drop, the diameter of the equivalent sphere computed as

$$d_{eq}^+ = \left(\frac{6V^+}{\pi}\right)^{1/3}, \tag{3.1}$$

where V^+ is the volume of the drop. Also reported in figure 4 is the Kolmogorov–Hinze scale, d_H^+, which can be computed as (Perlekar, Biferale & Sbragaglia 2012; Roccon *et al.* 2017; Soligo *et al.* 2019*a*)

$$d_H^+ = 0.725 \left(\frac{We}{Re_\tau}\right)^{-3/5} |\epsilon_c|^{-2/5}, \tag{3.2}$$

where ϵ_c is the turbulent dissipation, here evaluated at the channel centre where most of the drops collect because of their deformability (Lu & Tryggvason 2007; Soligo *et al.* 2020; Mangani *et al.* 2022). Although recently challenged (Qi *et al.* 2022; Vela-Martín & Avila 2022; Ni 2024), the Kolmogorov–Hinze scale (Kolmogorov 1941; Hinze 1955) still represents a convenient estimate to evaluate the critical diameter below which drop
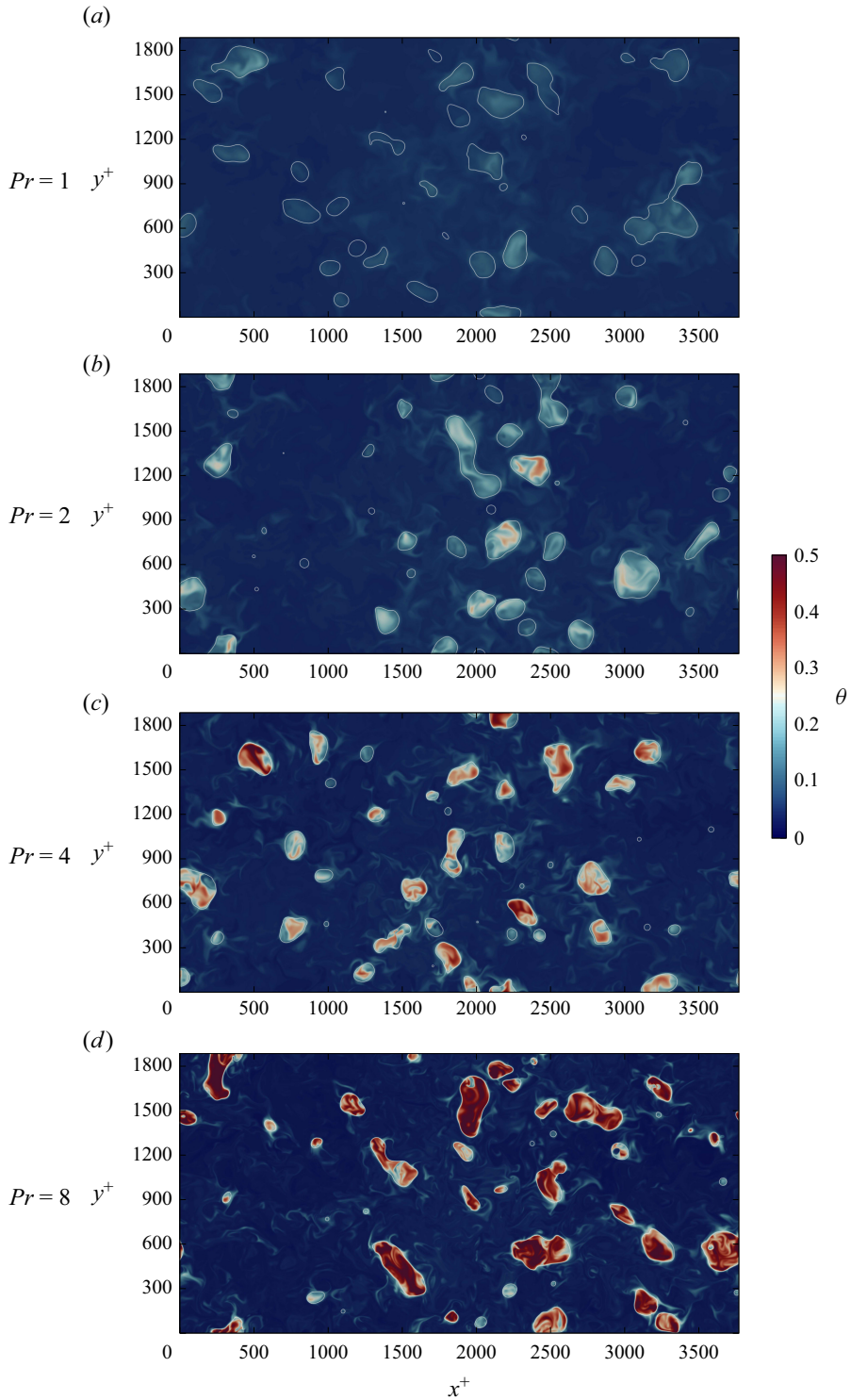
Figure 3. Instantaneous visualization of the temperature field (red, hot; blue, cold) on a $x^+ - y^+$ plane located at the channel centre for $t^+ = 1500$. Drop interfaces (iso-level $\phi = 0$) are reported using white lines. Each panel refers to a different Prandtl number. By increasing the Prandtl number (from top to bottom), the heat transfer becomes slower.
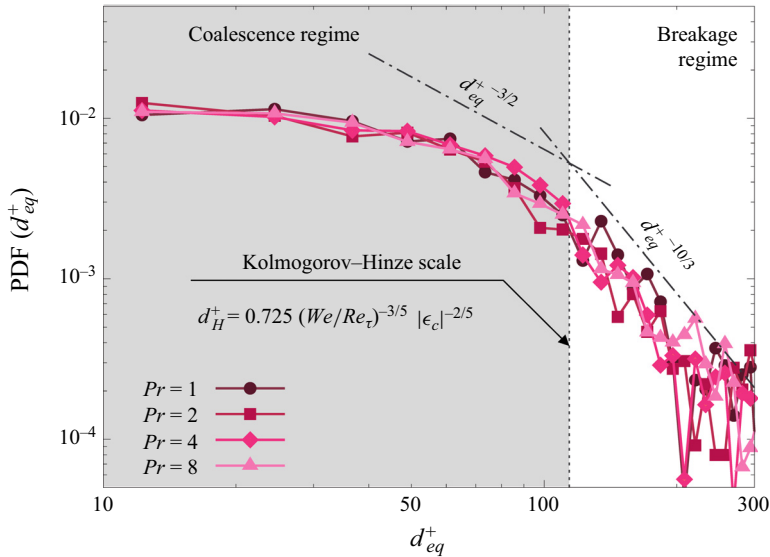
978 A12-12

Figure 4. Steady-state DSD obtained for: $Pr = 1$ (dark violet, circles), $Pr = 2$ (violet, squares), $Pr = 4$ (pink, diamonds) and $Pr = 8$ (light pink, triangles). The Kolmogorov–Hinze (KH) scale d_H^+ is reported with a vertical dashed line while the two analytical scaling laws, $d_{eq}^{+\,-3/2}$ for the coalescence-dominated regime (small drops, grey region) and $d_{eq}^{+\,-10/3}$ for the breakage-dominated regime (larger drops, white region), are reported with dash-dotted lines.

breakage is unlikely to occur. Based on the Kolmogorov–Hinze scale, we can identify two different regimes (Garrett, Li & Farmer 2000; Deane & Stokes 2002; Deike 2022). For drops smaller than the Kolmogorov–Hinze scale, we find the coalescence-dominated regime (left, grey area), in which drops that are smaller than the critical scale are generally not prone to break (although violent breakages can happen also for smaller drops). For drops larger than the Kolmogorov–Hinze scale, we find the breakage-dominated regime (right, white area) in which drop breakage is more likely to happen. Each regime is characterized by a specific scaling law, which describes the behaviour of the drop number density as a function of the drop size (Garrett *et al.* 2000; Deane & Stokes 2002; Chan, Johnson & Moin 2021): probability density function (PDF) $\sim d_{eq}^{+\,-3/2}$ below Kolmogorov–Hinze scale and PDF $\sim d_{eq}^{+\,-10/3}$ above it. The two scalings are represented by dot-dashed lines in figure 4.

We note that for equivalent diameters above the Hinze scale, our results follow quite well the theoretical scaling law and match the size distributions of the drops/bubbles obtained in the literature considering similar flow instances (Deike, Melville & Popinet 2016; Soligo, Roccon & Soldati 2021; Deike 2022; Di Giorgio, Pirozzoli & Iafrati 2022; Crialesi-Esposito, Chibbaro & Brandt 2023). Below the Hinze scale, for equivalent diameters in the range $25 < d_{eq}^+ < d_H^+$, our results match reasonably well the theoretical scaling law. For equivalent diameters $d_{eq}^+ < 25$ *w.u.*, we observe an underestimation of the DSD compared with the proposed scaling. This is linked to the grid resolution, and in particular to the problem in describing very small drops (Soligo *et al.* 2021; Roccon *et al.* 2023).
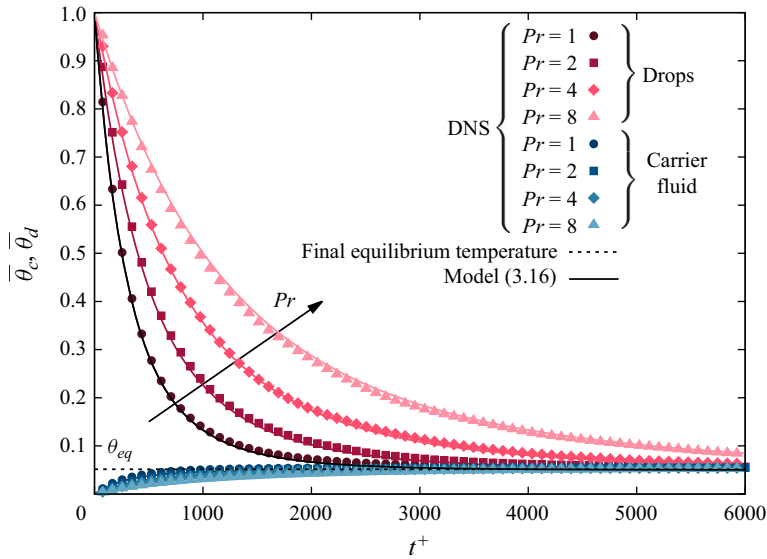
Figure 5. Time evolution of the mean temperature of drops (violet to pink colours, different symbols) and carrier fluid (blue to cyan colours, different symbols) for the different Prandtl numbers considered. DNS results are reported with full circles while the predictions obtained from the model are reported with continuous lines. The equilibrium temperature of the system, θ_{eq}, is reported with a horizontal dashed line.

3.3. *Mean temperature of drops and carrier fluid*

We now focus on the average temperature of the drops and of the carrier fluid. We consider the ensemble of all drops as one phase and the carrier fluid as the other phase (using the value of the phase field as a phase discriminator), and we compute the average temperature for each phase. The evolution in time of the drops and carrier fluid temperature, $\bar{\theta}_d$ and $\bar{\theta}_c$, respectively, is shown in figure 5 for the different values of Pr. Together with the results obtained by current DNS, filled symbols in figure 5, we also show the predictions obtained by a simplified phenomenological model (solid lines), the details of which will be described and discussed later (see § 3.4). We start considering the DNS results only. As expected, we observe that the average temperature of the drops (violet to pink symbols) decreases in time, while the average temperature of the carrier fluid (blue to cyan symbols) increases in time, until the thermodynamic equilibrium, at which both phases have the same temperature, is asymptotically reached. For this reason, simulations have been run long enough for the average temperature of both phases to be sufficiently close to the equilibrium temperature. In particular, we stopped the simulations at $t^+ \simeq 6000$, when the condition

$$\frac{(\bar{\theta}_d - \theta_{eq})}{(\theta_{d,0} - \theta_{eq})} \leq 0.05, \tag{3.3}$$

with $\theta_{d,0}$ the initial temperature of the drops, is satisfied by all simulations. The equilibrium temperature, θ_{eq}, can be easily estimated *a priori*: since the two walls are adiabatic and the homogeneous directions are periodic, the energy of the system is conserved over time. After some algebra and recalling the definition of volume fraction, $\Phi = V_d/(V_d + V_c)$, we obtain the equilibrium temperature:

$$\theta_{eq} = \theta_{c,0}(1 - \Phi) + \theta_{d,0}\Phi, \tag{3.4}$$

which is represented by the horizontal dashed line in figure 5.

978 A12-14

Figure 5 also provides a clear indication that a higher Prandtl number results in a longer time required for the system to reach the equilibrium temperature, θ_{eq}. The trend can be observed for both the drops and carrier fluid, as the two phases are mutually coupled (the heat released from the drops is adsorbed by the carrier fluid). This result confirms our previous qualitative observations, see figure 3 and discussion therein, where a large *Pr* (small thermal diffusivity) reduces the heat released by the drops. It is also interesting to observe that the behaviour of the mean temperature of the two phases appears self-similar at the different *Pr*.

3.4. *A phenomenological model for heat transfer rates in droplet laden flows*

In an effort to provide a possible interpretation of the previous results – and in particular to explain the average temperature behaviour shown in figure 5 – we develop a simple physically sound model of the heat transfer in drop-laden turbulence. We start by considering the heat transfer mechanisms from a single drop of diameter d^* to the surrounding fluid:

$$m_d^* c_p^* \frac{\partial \theta_d^*}{\partial t^*} = \mathcal{H}^* A_d^* (\theta_c^* - \theta_d^*), \tag{3.5}$$

where m_d^*, A_d^* and c_p^* are the mass, external surface and specific heat of the drop, $\mathcal{H}^*$ is the heat transfer coefficient, while θ_d^* and θ_c^* are the drop and carrier fluid temperature. The heat transfer coefficient can be estimated as the ratio between the thermal conductivity of the external fluid, λ^*, and a reference length scale, here represented by the thermal boundary layer thickness δ_t^*:

$$\mathcal{H}^* \sim \lambda^* / \delta_t^*. \tag{3.6}$$

With this assumption, and recalling that $\rho^* = \rho_c^* = \rho_d^*$, (3.5) becomes

$$\frac{\partial \theta_d^*}{\partial t^*} = \frac{6}{Pr} \frac{\nu^*}{d^* \delta_t^*} (\theta_c^* - \theta_d^*). \tag{3.7}$$

Reportedly (Schlichting & Gersten 2016, p. 218), the thermal boundary layer thickness, δ_t^*, can be expressed as $\delta_t^* = \delta^* Pr^{-\alpha}$, where δ^* is the momentum boundary layer thickness and α is an exponent that depends on the flow condition in the proximity of the boundary where the boundary layer evolves. In particular, the exponent α ranges from $\alpha = 1/3$ for no-slip conditions, usually assumed for solid particles, to $\alpha = 1/2$, usually assumed for clean gas bubbles. For an in-depth discussion on the topic, we refer the reader to Appendix A. As a consequence, the heat transfer rate observed from drops/bubbles is expected to be larger than that observed from solid particles, since the no-slip boundary condition generally weakens the flow motion near the interface (Levich 1962; Bird *et al.* 2002; Herlina & Wissink 2016). We can now rewrite the equation of the model in dimensionless form, using the initial drop-to-carrier fluid temperature difference $\Delta\theta^* = \theta_{d,0}^* - \theta_{c,0}^*$ as reference temperature, and ν^*/u_τ^{*2} as reference time:

$$\frac{\partial \theta_d}{\partial t^+} = 6 Re_\delta^{-1} Pr^{-1+\alpha} (d^+)^{-1} (\theta_c - \theta_d), \tag{3.8}$$

where d^+ is the drop diameter in wall units, while $Re_\delta = u_\tau^* \delta^* / \nu^*$ is the Reynolds number based on the boundary layer thickness (which can be assumed constant among the

different cases). Equation (3.8) can be rewritten as

$$\frac{\partial \theta_d}{\partial t^+} = \mathcal{C} Pr^{-1+\alpha}(d^+)^{-1}(\theta_c - \theta_d), \qquad (3.9)$$

where $\mathcal{C}$ is a constant whose value depends only on the flow structure, i.e. on Re_δ. Equation (3.9) describes the heat released by a single drop of dimensionless diameter d^+. Assuming now that the turbulent flow is laden with drops of different diameters, the general equation describing the heat released by the ith drop of diameter d_i^+ becomes

$$\frac{\partial \theta_{d,i}}{\partial t^+} = \mathcal{C} Pr^{-1+\alpha}(d_i^+)^{-1}(\theta_c - \theta_d) = \mathcal{F}_i, \qquad (3.10)$$

where $\mathcal{F}_i$ is the lumped-parameters representation of the right-hand side of the temperature evolution equation for the ith drop. As widely observed in the literature (Deane & Stokes 2002; Soligo *et al.* 2019*c*), and also confirmed by the present study (figure 4), we can hypothesize an equilibrium DSD by which the number density of drops scales as $d^{+-3/2}$ in the sub-Hinze range of diameters ($10 < d^+ < 110$), and as $d^{+-10/3}$ in the super-Hinze range of diameters ($110 < d^+ < 240$). With this approximation, and considering seven classes of drop diameter for the sub-Hinze range and four classes for the super-Hinze range, we can integrate (3.10) to obtain the time evolution of the temperature of each drop in time:

$$\theta_{d,i}^{n+1} = \theta_{d,i}^n + \Delta t^+ \mathcal{F}_i. \qquad (3.11)$$

From a weighted average of the temperature (based on the number of drops in each class, as per the theoretical DSD), we obtain the average temperature of the drops, $\bar{\theta}_d$.

To obtain the mean temperature of the carrier fluid, we consider that (adiabatic condition at the walls) the heat released by the drops is entirely absorbed by the carrier fluid. The heat released by the drops with a certain diameter d_i^* can be computed as

$$Q_i^* = m_d^* c_p^* \frac{\partial \theta_d}{\partial t^+} N_d^*(i), \qquad (3.12)$$

where $N_d^*(i)$ is the number of drops for that specific diameter (as per the DSD). The overall heat released by all drops can be calculated as the summation over all different classes of diameters:

$$Q_{tot}^* = \sum_{i=1}^{N_c} Q_i^*, \qquad (3.13)$$

where N_c is the employed number of classes. Finally, the mean temperature of the carrier fluid is

$$\bar{\theta}_c^{*,n+1} = \theta_c^{*,n} + \Delta t^+ \frac{Q_{tot}^*}{m_c^* c_p^*}. \qquad (3.14)$$

In dimensionless form (dividing by the initial drop-to-carrier fluid temperature $\Delta \theta^*$), (3.14) becomes

$$\bar{\theta}_c^{n+1} = \theta_c^n + \Delta t^+ Q_{tot}. \qquad (3.15)$$

The results of the model are shown in figure 5. Interestingly, under the simplified hypothesis of the model (chiefly, the spherical shape of the drops, constant DSD evaluated
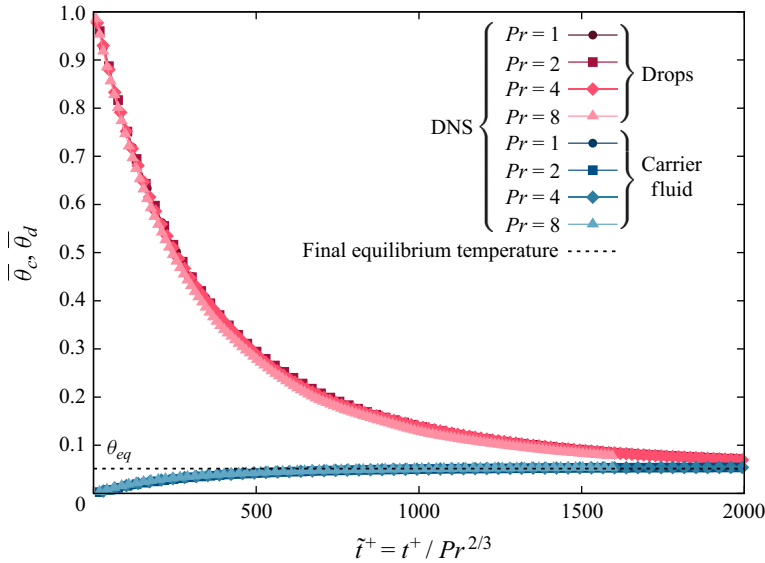
978 A12-16

Figure 6. Time evolution of the mean temperature of drops (violet to pink colours) and carrier fluid (blue to cyan colours) for the different Prandtl numbers considered obtained from DNS and reported against the dimensionless time $\tilde{t}^+ = t^+/Pr^{2/3}$. The equilibrium temperature of the system, θ_{eq}, is reported with a horizontal dashed line. The DNS results reported over the new dimensionless time nicely collapse on top of each other, highlighting the self-similarity of the $\bar{\theta}_{c,d}$ profiles.

at the equilibrium), we observe that the behaviour of the mean temperature is very well captured by the model (represented by the solid lines in figure 5):

$$\frac{\partial \theta_d}{\partial t^+} = \mathcal{C}Pr^{-2/3}(d^+)^{-1}(\theta_c - \theta_d), \tag{3.16}$$

i.e. when $\alpha = 1/3$ – typical of boundary layers around solid objects (i.e. solid particles). Reasons for this behaviour might be traced back to the weakening of convective phenomena induced by the interface of the drops (Scarbolo & Soldati 2013). This effect is more pronounced at the beginning of the simulation when large drops are not yet present. In addition, it must be also noticed that drops are strongly advected by the mean flow, and the flow condition at the drop surface can be different from the slip one and is, in general, not of simple evaluation. Given the relationship $\partial \theta_d/\partial t \sim Pr^{-2/3}$ postulated by the model in (3.16), which provides results in very good agreement with the numerical ones, it seems reasonable to rescale the time variable as

$$\tilde{t}^+ = \frac{t^+}{Pr^{(1-\alpha)}} = \frac{t^+}{Pr^{(2/3)}}. \tag{3.17}$$

A representation of the DNS results in terms of the rescaled time, (3.17), is shown in figure 6. We observe a nice collapse of the two sets of curves – drops and carrier fluid (red and blue) – for the different values of Pr, which clearly demonstrates the self-similar behaviour of $\bar{\theta}$. For this reason, the rescaling of time $\tilde{t}^+ = t^+/Pr^{2/3}$ will be also used in the following.

978 A12-17

3.5. *Heat transfer from particles and drops/bubbles*

It is now important to discuss the behaviour of the heat transfer coefficient (and its dimensionless counterpart, the Nusselt number *Nu*) also in the context of available literature results. Naturally, similar considerations can be made to evaluate the mass transfer coefficient, in particular at liquid/gas interfaces (Levich 1962; Bird *et al.* 2002).

For solid particles, a balance between the convective time scale near the surface and the diffusion time scale gives a heat transfer coefficient (Krishnamurthy & Subramanian 2018),

$$\mathcal{H}^* \propto Pr^{-2/3}, \tag{3.18}$$

and the corresponding Nusselt number,

$$Nu \propto Re^{\beta} Pr^{1/3}, \tag{3.19}$$

where β is an exponent that depends on the flow conditions and links the boundary layer thickness to the particle Reynolds number. Usually, $\beta = 1/3$ for small Reynolds numbers (Krishnamurthy & Subramanian 2018), while $\beta = 1/2$ for large Reynolds numbers (Ranz 1952; Whitaker 1972; Michaelides 2003).

Using similar arguments (balance between convective and diffusion time scales), but considering now that at the surface of a drop/bubble, a slip velocity, and therefore a certain degree of advection, can be observed (Levich 1962; Bird *et al.* 2002; Herlina & Wissink 2016), the heat transfer coefficient is found to scale as

$$\mathcal{H}^* \propto Pr^{-1/2}, \tag{3.20}$$

and the corresponding Nusselt number as

$$Nu \propto Re^{\beta} Pr^{1/2}, \tag{3.21}$$

where also in this case, the exponent β does depend on the considered Reynolds number. Two regimes are usually defined (Theofanous, Houze & Brumfield 1976): a low-Reynolds-number regime, for which $\beta = 1/2$, and a high-Reynolds-number regime, for which $\beta = 3/4$. An alternative approach, which gives similar predictions, is to use the penetration theory of Higbie (1935), in which turbulent fluctuations are invoked to estimate a flow exposure (or contact) time to compute the heat/mass transfer coefficient. Such an approach has been widely used in bubble-laden flows (Colombet *et al.* 2011; Herlina & Wissink 2014, 2016; Farsoiya *et al.* 2021).

We can now evaluate the heat transfer coefficient from our DNS at different *Pr*, and compare it to the proposed scaling laws. Note that the heat transfer coefficient is obtained as

$$\mathcal{H} = \frac{(\bar{\theta}_d^{n+1} - \bar{\theta}_d^n)}{A \Delta t (\bar{\theta}_d^{n+1/2} - \bar{\theta}_c^{n+1/2})}, \tag{3.22}$$

where the numerator represents the temperature difference of the drops between the time steps n and $n + 1$, while the denominator represents the temperature difference between the drop and the carrier fluid evaluated halfway in time between step n and $n + 1$ (i.e. at $n + 1/2$). The quantity A is the total interfacial area between drops and carrier fluid, while Δt is the time step used to evaluate the heat transfer. Here, we have evaluated the heat transfer coefficient taking the heat released by the drops as a reference; an equivalent result, but with the opposite sign, can be obtained using the heat absorbed by the carrier fluid as a reference, and taking into account the different volume fraction of the two phases.
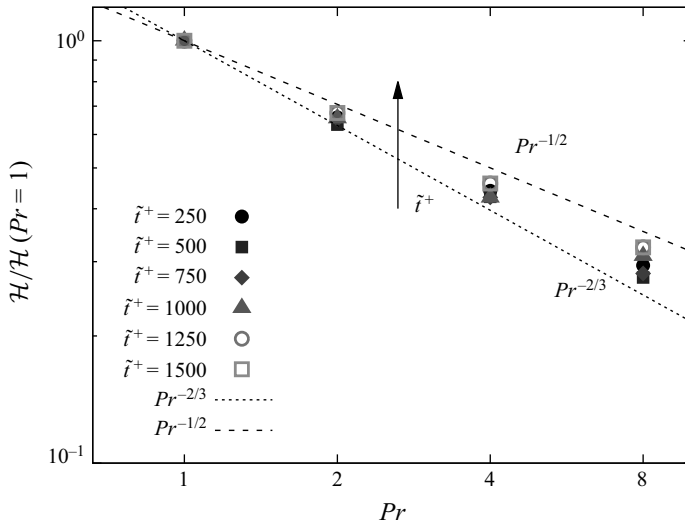
Figure 7. Time behaviour of the dimensionless heat transfer coefficient for the different Prandtl numbers considered. The results are compared for different values of the newly defined dimensionless time $\tilde{t}^+ = t^+/Pr^{2/3}$. Heat transfer coefficients are reported normalized by the value of the heat transfer coefficient obtained for $Pr = 1$ (at the same time instant $\tilde{t}^+$). In this way, results obtained at different time instants can be conveniently compared. The two scaling laws that refer to $\alpha = 2/3$ and $\alpha = 1/2$ are also reported as references.

The dimensionless heat transfer coefficient, (3.22), is shown as a function of Pr, and at different time instants (based on the dimensionless time $\tilde{t}^+$, (3.17)), in figure 7. Further details on the time evolution of $\mathcal{H}$ are given in Appendix B. For a better comparison, the results are normalized by the value of the heat transfer coefficient for $Pr = 1$. The two reference scaling laws, $\mathcal{H} \sim Pr^{-2/3}$ obtained for $\alpha = 1/3$ and $\mathcal{H} \sim Pr^{-1/2}$ obtained for $\alpha = 1/2$, are also shown by a dotted and a dashed line. We note that at the beginning of the simulations (see for example $\tilde{t}^+ = 250$), the heat transfer coefficient is close to $\mathcal{H} \sim Pr^{-2/3}$, while at later times, it tends towards $\mathcal{H} \sim Pr^{-1/2}$, hence approaching the scaling law proposed for heat/mass transfer in gas–liquid flows (Levich 1962; Magnaudet & Eames 2000; Bird *et al.* 2002; Herlina & Wissink 2014, 2016; Colombet *et al.* 2018; Farsoiya *et al.* 2021).

A possible explanation is that, as time advances, the shape of the drops becomes complex and coalescence/breakups more frequent, thus inducing a higher degree of internal mixing that is associated with a heat transfer increase. This is reflected in a heat transfer process that is slower at the beginning, $\mathcal{H}^* \sim Pr^{-2/3}$, and faster at later times, $\mathcal{H}^* \sim Pr^{-1/2}$.

3.6. *Influence of the drop size on the average drop temperature*

In the previous sections, we have studied the behaviour of the mean temperature field of the drops and of the carrier fluid considered as single entities. However, while this description is perfectly reasonable for the carrier fluid – which can be considered a continuum – it can be questionable for the drops, which are not a continuum phase by nature. We now take the dispersed nature of the drops into account and we evaluate, for each drop, the equivalent diameter and the corresponding mean temperature.

This is sketched in figure 8, where the average temperature of each drop (represented by a dot) is shown as a function of its equivalent diameter, at different time instants (between $t^+ = 1050$ and $t^+ = 2400$). Each panel refers to a different Prandtl number. Note that at
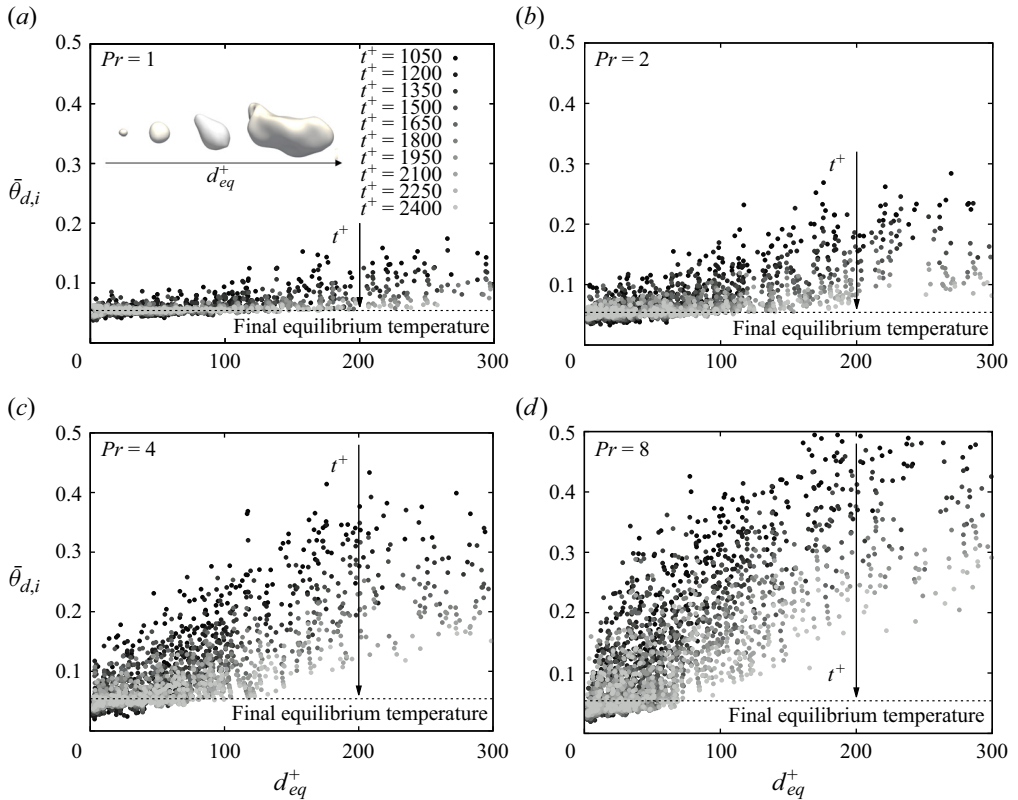
Figure 8. Scatter plot of the drop equivalent diameter d_{eq}^+ against the drop average temperature, $\bar{\theta}_{d,i}$. Each dot represents a different drop while its colour (black to grey colour map) identifies different times, from $t^+ = 1050$ (black) up to $t^+ = 2400$ (grey). Each panel refers to a different Prandtl number. A sketch showing drops of different equivalent diameters is reported in the upper part of (*a*).

$t^+ = 2400$, the case $Pr = 1$ has almost reached the thermodynamic equilibrium (figure 5). It is clearly visible that regardless of the considered time, small drops have an average temperature close to the equilibrium one. This is particularly visible at smaller Prandtl numbers, i.e. when heat transport is faster, but it can be observed also at larger Pr. In contrast, the average temperature of larger drops is larger. Hence, the average temperature of the drops seems directly proportional to the drop size, as can be argued considering that the heat released by the drop, and hence its temperature reduction, is $\partial \theta_d / \partial t \propto d^{-1}$ (3.14). It is therefore not surprising that the scatter plot at a given time instant is characterized by dots distributing in a stripes-like fashion, with a slope that decreases with time. This behaviour is observed at all Pr, although the range of drops temperature (y axis) at small Pr is definitely narrower (because of their larger heat loss) compared to that at large Pr. It is also interesting to note – in particular, at $Pr = 4$ and $Pr = 8$ in panels (*c*,*d*) – the presence of drops with a temperature smaller than the equilibrium one (dots falling below the horizontal line that marks the equilibrium temperature). We can link this behaviour to the small relaxation time of small drops that therefore adapt quickly to the local temperature of the carrier fluid, which can be smaller than the equilibrium one for two main reasons. First, at the early stages of the simulations and at high Prandtl numbers, the temperature of the carrier fluid is lower than the equilibrium one. Second, temperature fluctuations (of both negative and positive signs) are present also in the carrier fluid.
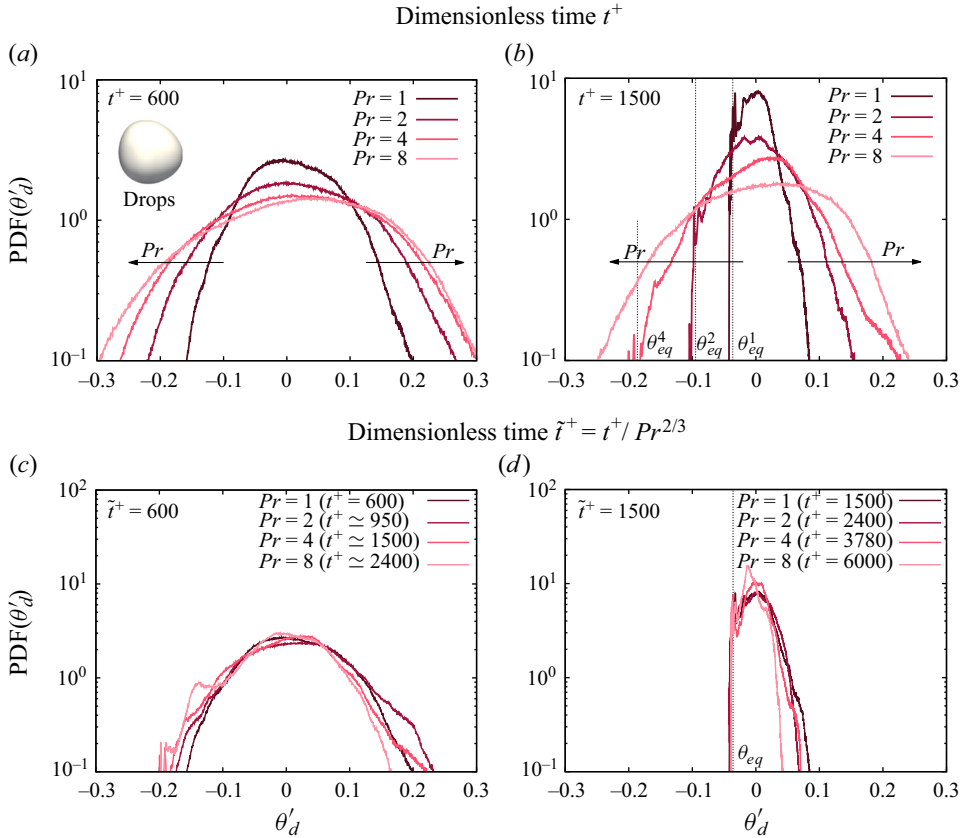
978 A12-20

Figure 9. The PDF of the temperature fluctuations, $\theta'_d = \theta_d - \bar{\theta}_d$ inside the drops. Each case is reported with a different color (violet to light pink) depending on the Prandtl number. The PDFs obtained at two different time instants: (a) $t^+ = 600$ and (b) $t^+ = 1500$. The PDFs obtained at two rescaled time instants: (c) $\tilde{t}^+ = 600$ and (d) $\tilde{t}^+ = 1500$, where the rescaled time is computed as $\tilde{t}^+ = t^+/Pr^{2/3}$. For (c,d), the corresponding t^+ is reported between brackets.

These fluctuations, in the form of hot/cold striations, are more likely observed at large Pr (see the striation-like structures at $Pr = 8$ in figure 3d).

3.7. *Temperature fluctuations inside the drops*

In many applications, in particular, to evaluate mixing efficiency and flow homogeneity, not only is the average temperature of drops important, but also its space and time distribution inside the drops. To understand it, we now look at the PDF of the temperature fluctuations inside the drops,

$$\theta'_d = \theta_d - \overline{\theta}_d, \tag{3.23}$$

where θ_d is the local temperature inside the drop and $\bar{\theta}_d$ is the average temperature of all drops at a certain time (as per figure 5). Results are shown in figure 9. Figure 9(a,b) shows the PDF of θ'_d at different Pr, and at two different time instants: (a) $t^+ = 600$ and (b) $t^+ = 1500$. Figure 9(c,d) shows the PDFs obtained at two different rescaled time instants, $\tilde{t}^+ = t^+/Pr^{2/3}$: (c) $\tilde{t}^+ = 600$ and (d) $\tilde{t}^+ = 1500$.

Considering first figure 9(*a*) ($t^+ = 600$), we notice that all PDFs have a rather regular shape, characterized by the presence of both positive and negative fluctuations (with respect to the average temperature), with a slight asymmetry towards the positive ones (positive fluctuations are more likely observed). A comparison between the curves obtained at different *Pr* shows that the range of temperature fluctuations is wider at larger *Pr*. This is due to the small thermal diffusivity at large *Pr*, which allows temperature fluctuations in the drop to survive much longer before they are damped and spread by diffusion. Naturally, at later times (figure 9*b*, $t^+ = 1500$), the range of temperature fluctuations reduces. Indeed, as heat is transferred from the drops to the carrier fluid, the maximum temperature of drops reduces and so does the range of temperature fluctuations inside the drop. This trend is more pronounced for negative fluctuations, as the minimum temperature inside the drops is somehow bounded by the temperature of the carrier fluid (which increases only a little, from $\bar{\theta}_{c,0} = 0$ to $\theta_{eq} = 0.054$, during the simulation). This latter observation is visible in the shape of the PDFs at $Pr = 1$, 2 and 4, since the system is closer to the thermal equilibrium at this time instant (the thermal equilibrium is identified in panel *b* by a vertical dashed line and marked with a label, θ_{eq}^{Pr}): a sharp drop of the PDF, which does not significantly trespass the θ_{eq}^{Pr} limit, is observed. In contrast, positive temperature fluctuations are subject to relatively weaker constraints (they are only bounded by the maximum initial temperature of the drops). This results in a PDF that gets asymmetric, positively skewed. It is also interesting to observe the development of a pronounced peak about the equilibrium temperature θ_{eq}^{Pr}, which corresponds to the presence of small drops (generated by breakages events) that – given their small thermal relaxation time and heat capacity – almost immediately adapt to the equilibrium temperature (see also figure 2*d*,*f*).

However, a discussion on the temperature fluctuations, captured from flows at different *Pr* and after the same time t^+ from the initial condition, could be misleading because it puts in contrast flows at different thermal states (i.e. different average temperatures and different temperature gradients, see figure 5). To filter out this effect, we compute the PDFs of the temperature fluctuations at the same rescaled time instants $\tilde{t}^+ = t^+/Pr^{2/3}$. By doing this, all cases can be considered at similar thermal conditions (see also figure 6). The resulting PDFs, at $\tilde{t}^+ = 600$ and $\tilde{t}^+ = 1500$, are shown in figure 9(*c*,*d*). Note that for the sake of clarity, the corresponding t^+, which is different from case to case, is reported between brackets in the legend. In the rescaled time units, the collapse between the different curves is quite nice. The slight difference between the curves is due to the fact that, although the system is at the same thermal state (same $\tilde{t}^+$), it is at a different flow state (different t^+), i.e. the instantaneous DSDs are different. This gives the slightly larger negative fluctuations at larger *Pr* (which, being at a later stage, is characterized by the presence of smaller and colder drops), and slightly larger positive fluctuations at smaller *Pr* (which, being at an earlier flow state, is characterized by the presence of larger and warmer drops).

From a closer look at figure 9(*d*) ($\tilde{t}^+ = 1500$), we note very clearly the constraint set by the thermal equilibrium condition: the PDF cannot significantly trespass the limit represented by θ_{eq} (vertical dashed line), which is very similar for all *Pr*, given the similar thermal state. Also visible is the peak, already discussed in figure 9(*b*), which emerges very close to the equilibrium temperature θ_{eq} and that is due to the presence of small drops that adapt quickly to the local temperature of the carrier fluid. As previously noticed in figure 9(*c*), the higher probability of finding small drops at lower *Pr* is also responsible for the narrowing of the PDF (reduction of positive temperature fluctuations).

4. Conclusions

In this work, we studied heat transfer in a turbulent channel flow laden with large and deformable drops. The drops are initially warmer than the carrier fluid and as the simulations advance, heat is transferred from the drops to the carrier fluid. Simulations considered a fixed value of the Reynolds number, $Re_\tau = 300$, and Weber number, $We = 3$, and analysed different Prandtl number values, from $Pr = 1$ to $Pr = 8$. The Prandtl number is changed by changing the thermal diffusivity. The investigation is based on the DNS of turbulent heat transfer, coupled with a PFM used to describe interfacial phenomena. First, we focused on the drop dynamics, observing that after an initial transient (up to $t^+ = 1000$), the DSD reaches a quasi-equilibrium condition where it follows the scaling $d_{eq}^{+\ -3/2}$ in the coalescence-dominated regime and $d_{eq}^{+\ -10/3}$ in the breakage-dominated regime. The threshold between the coalescence-dominated and the breakage-dominate regimes is represented by the Kolmogorov–Hinze scale. Then, we characterize the behaviour of the average temperature of the drops and of the carrier fluid: as expected, the average temperature of drops decreases in time, while the average temperature of the carrier fluid increases in time, until reaching the equilibrium condition of uniform temperature in the whole system. We clearly observed that a higher Prandtl number results in a longer time required for the system to reach the equilibrium temperature. Interestingly, the time behaviour of the temperature profiles of both drops and carrier fluid is self-similar. Building on top of these numerical results, we developed a phenomenological model that can accurately reproduce the time evolution of the mean temperatures at all Prandtl numbers considered here. This model gave us the opportunity to introduce a new self-similarity variable (time, $\tilde{t}^+$) that accounts for the Prandtl number effect, and by which all results collapse on a single curve. In addition, we also computed the heat transfer coefficient $\mathcal{H}$ (and its dimensionless counterpart, the Nusselt number Nu) and showed that it scales as $\mathcal{H} \sim Pr^{-2/3}$ (which corresponds to a Nusselt number scaling $Nu \sim Pr^{1/3}$) at the beginning of the simulation, and tends to $\mathcal{H} \sim Pr^{-1/2}$ (or alternatively, $Nu \sim Pr^{1/2}$) at later times. These different scalings are consistent with previous literature predictions and can be explained via the boundary layer theory ([Appendix A](#)). The effects of the Prandtl number on the temperature distribution inside the drops have been investigated. We observe that by increasing the Prandtl number, the PDFs become wider and thus large temperature fluctuations are more likely to be observed. Interestingly, when the PDFs are compared at the same rescaled time $\tilde{t}^+$ (i.e. accounting for the Prandtl number effect), all curves collapse on top of each other, with only minor differences possibly due to the different instantaneous DSD. The effect of the drop size was also discussed: small drops adapt faster to the equilibrium temperature, thanks to their small heat capacity, compared to larger drops. Finally, it must be pointed out that since the different phases of a multiphase flow can have different thermophysical properties, Prandtl numbers can be also different from phase to phase. This aspect, which was not considered in the present work, will be the topic of a future study. In addition, in the present work, we have assumed a constant and uniform surface tension. However, in many circumstances, surface tension does depend on temperature, therefore inducing thermocapillary effects. This will also be the subject of a future investigation.

F. Mangani, A. Roccon, F. Zonta and A. Soldati

Author ORCIDs.
- Francesca Mangani https://orcid.org/0000-0001-7777-6665;
- Alessio Roccon https://orcid.org/0000-0001-7618-7797;
- Francesco Zonta https://orcid.org/0000-0002-3849-315X;
- Alfredo Soldati https://orcid.org/0000-0002-7515-7147.

Appendix A. Effects of slip condition on the velocity and thermal boundary layer evolution

In this section, we derive and solve the equations that describe the evolution of the boundary layer on a heated flat plate that is parallel to a constant unidirectional flow.

In addition to the standard description of the boundary layer, where no-slip conditions on the plate are considered (Prandtl 1905; Blasius 1908), here we consider also the effect of a slip velocity on the velocity and thermal boundary layers (Martin & Boyd 2006; Bhattacharyya, Mukhopadhyay & Layek 2011; Aziz, Siddique & Aziz 2014). Following the standard approach (Schlichting & Gersten 2016), the continuity, Navier–Stokes and energy equations in 2-D are

$$\frac{\partial u}{\partial x} + \frac{\partial v}{\partial y} = 0, \tag{A1}$$

$$u\frac{\partial u}{\partial x} + v\frac{\partial u}{\partial y} = -\frac{1}{\rho}\frac{\partial p}{\partial x} + v\frac{\partial^2 u}{\partial y^2}, \tag{A2}$$

$$u\frac{\partial T}{\partial x} + v\frac{\partial T}{\partial y} = a\frac{\partial^2 T}{\partial y^2}, \tag{A3}$$

where x is the direction parallel to the wall and y the direction normal to the wall, see figure 10. The boundary conditions, accounting also for the slip velocity, read as

$$u(x, y = 0) = k\frac{\partial u}{\partial y}(x, y = 0), \tag{A4}$$

$$v(x, y = 0) = 0, \tag{A5}$$

$$u(x, y \to +\infty) = u_\infty, \tag{A6}$$

$$T(x, y = 0) = T_w, \tag{A7}$$

$$T(x, y \to +\infty) = T_\infty, \tag{A8}$$

where k is a parameter that controls the amount of slip at the wall (no-slip for $k = 0$, up to free-slip for $k \to +\infty$), u_∞ and T_∞ are the free stream velocity and temperature, and T_w is the constant temperature of the flat plate. To solve the system of equations, we use the method of similarity transformation. First, we consider the continuity and Navier–Stokes equations. Following Blasius (1908), we introduce the following similarity

transformation:

$$\eta = y\sqrt{\frac{u_\infty}{\nu x}}. \tag{A9}$$

We can define a dimensionless stream function, $f(\eta)$, which depends only on the variable η, as

$$f(\eta) = \frac{\psi(x, y)}{\sqrt{u_\infty \nu x}}, \tag{A10}$$

from which we can express the two dimensionless velocity components:

$$\frac{u}{u_\infty} = f'; \quad \frac{v}{u_\infty} = \frac{1}{2}\sqrt{\frac{u_\infty \nu}{x}}(\eta f' - f), \tag{A11a,b}$$

where f' denotes the first derivative with respect to η (the same notation is used for higher-order derivatives). Upon substitution of these variables in the continuity and Navier–Stokes equations, we obtain the governing equation for the dimensionless stream function $f(\eta)$:

$$f''' + \tfrac{1}{2}ff'' = 0, \tag{A12}$$

together with the boundary conditions

$$f'(\eta = 0) = kf''(\eta = 0), \tag{A13}$$

$$f(\eta = 0) = 0, \tag{A14}$$

$$f'(\eta \to +\infty) = 0. \tag{A15}$$

Considering now the energy equation for the dimensionless temperature θ,

$$\theta = \frac{T - T_\infty}{T_w - T_\infty}, \tag{A16}$$

and using the similarity transformation, the governing equation for the dimensionless temperature becomes

$$\theta'' + \tfrac{1}{2}Prf\theta' = 0, \tag{A17}$$

where $Pr = \nu/\alpha$ is the Prandtl number, and the following boundary conditions are applied:

$$\theta(\eta = 0) = 1, \tag{A18}$$

$$\theta(\eta \to +\infty) = 0. \tag{A19}$$

The governing equations (A12) and (A17), which constitute a boundary value problem, are solved numerically via a shooting method which, avoiding the imposition of the boundary condition (A6), stabilizes the computation over a wider range of η. The equations are solved for different values of k, from $k = 0$ (no-slip) up to $k = 5$, at which the velocity at the wall ($\eta = 0$) is $\simeq 70\%$ of the free stream velocity. The resulting velocity profiles (rotated by $90°$ to be consistent with the sketch of figure 10) are shown in figure 11 for different values of k. Panel (*a*) shows the effect of k on the streamwise component of the velocity, while panel (*b*) shows the effect of k on the temperature profile. All the results refer to $Pr = 1$, for which the temperature solution can be obtained as $\theta = 1 - f'$. For the no-slip case ($k = 0$), the Blasius solution (velocity and temperature, shown by the red circles) is recovered. As expected, by increasing k, the amount of slip at the plate
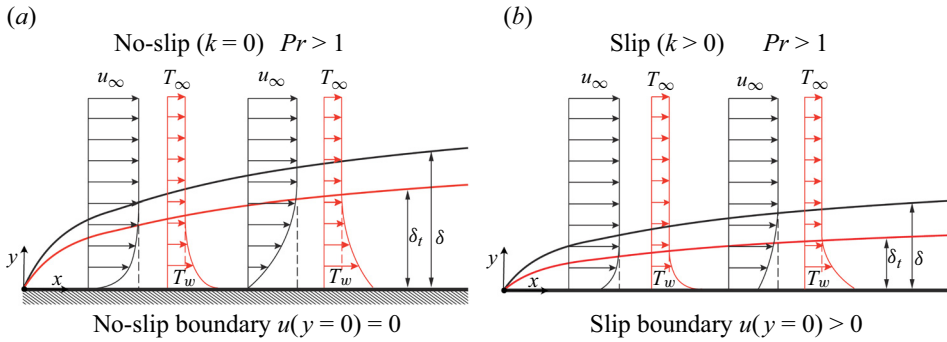
Figure 10. Sketch of the momentum and thermal boundary layer dynamics on a flat plate characterized by a uniform temperature, T_w, larger than the free stream temperature, T_∞. In (*a*), no-slip conditions are enforced at the wall (corresponding to a slip parameter $k = 0$), while in (*b*), partial slip is allowed at the wall. The qualitative behaviour of the momentum and thermal boundary layer thickness is also shown for the two cases. Both panels refer to a super-unitary Prandtl number.
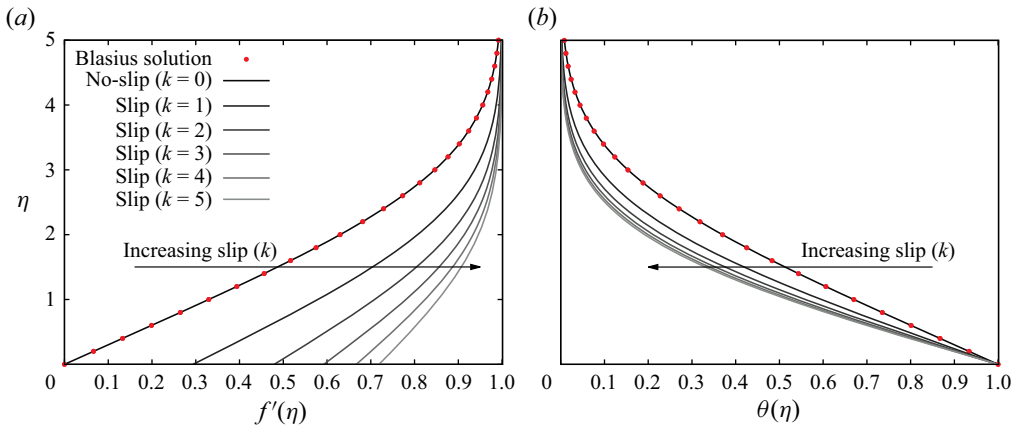

Figure 11. (*a*) Streamwise velocity and (*b*) temperature profiles obtained for different values of the slip parameter $k = 0$. Results are reported rotated by $90°$ for the sake of better interpretation and are obtained considering $Pr = 1$. For the no-slip case ($k = 0$), the classical Blasius solution available in archival literature for the velocity, f', and temperature, $\theta = 1 - f'$, is reported with red dots. By increasing the slip parameter k, the velocity at the wall location $\eta = 0$ increases and larger temperature gradients are observed.

increases. As a consequence, the temperature profiles are also modified, generating larger temperature gradients at the plate. This corresponds to a heat transfer increase, as also observed in previous studies (Martin & Boyd 2006; Aziz *et al.* 2014).

Of specific importance, in the context of the model developed in the present paper, is the evaluation, as a function of the slip parameter k and for different values of Pr, of the ratio between the velocity and the thermal boundary layer thickness, respectively defined as (Martin & Boyd 2006)

$$\delta = \int_0^{+\infty} (1 - f') \, \mathrm{d}\eta \quad \text{and} \quad \delta_t = \int_0^{+\infty} \theta \, \mathrm{d}\eta. \qquad (A20a,b)$$

The ratio δ_t/δ is shown in figure 12 as a function of Pr and for different values of the slip parameter k (different symbols). We notice that when the no-slip condition is enforced
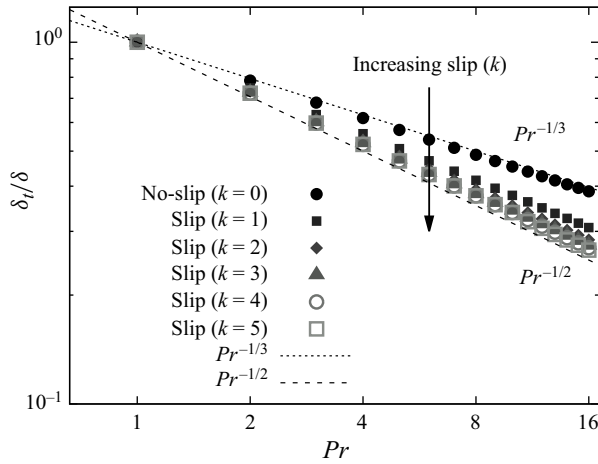
978 A12-26

Figure 12. Ratio between the thermal and momentum boundary layer thickness as a function of the Prandtl number and the slip parameter k. The scaling laws $Pr^{-1/3}$ and $Pr^{-1/2}$ are reported as reference. Moving from $k = 0$ (no-slip) to $k = 5$ (slip), for a given value of the Prandtl number, the thermal boundary layer becomes thinner thus leading to an increase of the heat transferred from the wall.

($k = 0$), the ratio $\delta_t/\delta \sim Pr^{-1/3}$, in agreement with the thermal boundary layer theory on flat plates (Schlichting & Gersten 2016). However, when a slip condition is introduced at the wall ($k > 0$), the ratio δ_t/δ relaxes onto the scaling $\delta_t/\delta \sim Pr^{-1/2}$. This indicates that at a given Pr, the thermal boundary layer for the slip case becomes thinner compared to the no-slip case, and the heat transfer increases. In other words, heat transfer coefficients for drops/bubbles (slip surfaces) can be higher compared to the corresponding values for solid particles (no-slip surfaces) (Herlina & Wissink 2016). In particular, based on the previous observations and on the model developed in § 3.4, we can obtain the following scalings for the heat transfer coefficients:

$$\mathcal{H}^* \propto Pr^{-2/3} \quad \text{for no-slip,} \tag{A21}$$

$$\mathcal{H}^* \propto Pr^{-1/2} \quad \text{for free-slip.} \tag{A22}$$

Appendix B. Time evolution of the heat transfer coefficient

In this section, we report the time evolution of the heat transfer coefficient $\mathcal{H}$, evaluated as per (3.22), for the different values of the Prandtl number Pr considered here. Results are shown in figure 13 as a function of the dimensionless time $\tilde{t}^+ = t^+/Pr^{2/3}$.

Considering figure 13(*a*), we can observe that the heat transfer coefficient exhibits a self-similar behaviour, and after an initial transient (after $\tilde{t} > 1000$), it attains a steady-state condition for all the different cases. Upon rescaling of the heat transfer coefficient $\mathcal{H}$ by the factor $Pr^{2/3}$, we observe a fair collapse of all curves on top of each other. Some minor differences are perhaps observed at high Prandtl numbers. Note indeed that at high Prandtl numbers, the curves become a bit more noisy, as the rescaling factor amplifies the fluctuations of the heat transfer coefficient.
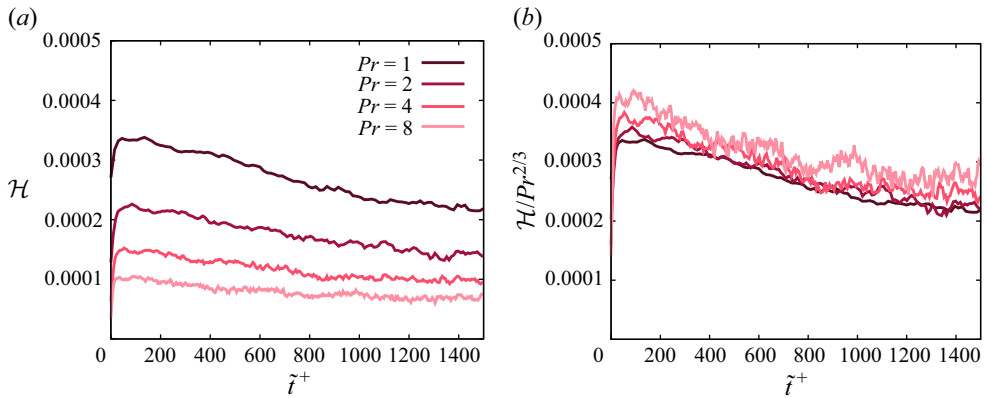
Figure 13. Time evolution of the heat transfer coefficient as a function of the dimensionless time $\tilde{t}^+ = t^+/Pr^{2/3}$ for the different Prandtl numbers considered. In (a), the heat transfer is shown as per (3.22), while in (b), it is rescaled by the factor $Pr^{2/3}$.

REFERENCES

AKSNES, D.L. & EGGE, J.K. 1991 A theoretical model for nutrient uptake in phytoplankton. *Mar. Ecol. Prog. Ser. Oldendorf* **70** (1), 65–72.

ALBERNAZ, D.L, DO-QUANG, M., HERMANSON, J.C. & AMBERG, G. 2017 Droplet deformation and heat transfer in isotropic turbulence. *J. Fluid Mech.* **820**, 61–85.

ANTONIA, R.A. & ORLANDI, P. 2003 Effect of Schmidt number on small-scale passive scalar turbulence. *Appl. Mech. Rev.* **56** (6), 615–632.

ASHGRIZ, N. 2011 *Handbook of Atomization and Sprays: Theory and Applications*. Springer Science & Business Media.

AZIZ, A., SIDDIQUE, J.I. & AZIZ, T. 2014 Steady boundary layer slip flow along with heat and mass transfer over a flat porous plate embedded in a porous medium. *PLoS ONE* **9** (12), e114544.

BADALASSI, V.E., CENICEROS, H.D. & BANERJEE, S. 2003 Computation of multiphase systems with phase field models. *J. Comput. Phys.* **190** (2), 371–397.

BATCHELOR, G.K. 1959 Small-scale variation of convected quantities like temperature in turbulent fluid. Part 1. General discussion and the case of small conductivity. *J. Fluid Mech.* **5** (1), 113–133.

BATCHELOR, G.K., HOWELLS, I.D. & TOWNSEND, A.A. 1959 Small-scale variation of convected quantities like temperature in turbulent fluid. Part 2. The case of large conductivity. *J. Fluid Mech.* **5** (1), 134–139.

BHATTACHARYYA, K., MUKHOPADHYAY, S. & LAYEK, G.C. 2011 Steady boundary layer slip flow and heat transfer over a flat porous plate embedded in a porous media. *J. Petrol. Sci. Engng* **78** (2), 304–309.

BIRD, R.B., STEWART, W.E. & LIGHTFOOT, E.N. 2002 *Transport Phenomena*. Wiley.

BIROUK, M. & GÖKALP, I. 2002 A new correlation for turbulent mass transfer from liquid droplets. *Intl J. Heat Mass Transfer* **45** (1), 37–45.

BIROUK, M. & GÖKALP, I. 2006 Current status of droplet evaporation in turbulent flows. *Prog. Energy Combust. Sci.* **32** (4), 408–423.

BLASIUS, H. 1908 Grenzschichten in flussigkeiten mit kleiner Reibung (English translation), *NACA Tech. Rep.* TM 1256.

BOTHE, D., KOEBE, M., WIELAGE, K., PRÜSS, J. & WARNECKE, H.-J. 2004 *Direct Numerical Simulation of Mass Transfer between Rising Gas Bubbles and Water*. Springer.

BOUSSINESQ, J. 1905 Calcul du pouvoir refroidissant des courants fluides. *J. Math. Pures Appl.* **1**, 285–332.

BOYD, B. & LING, Y. 2023 A consistent volume-of-fluid approach for direct numerical simulation of the aerodynamic breakup of a vaporizing drop. *Comput. Fluids* **254**, 105807.

CHAN, W.H.R., JOHNSON, P.L. & MOIN, P. 2021 The turbulent bubble break-up cascade. Part 1. Theoretical developments. *J. Fluid Mech.* **912**, A42.

CHONG, K.L., NG, C.S., HORI, N., YANG, R., VERZICCO, R. & LOHSE, D. 2021 Extended lifetime of respiratory droplets in a turbulent vapor puff and its implications on airborne disease transmission. *Phys. Rev. Lett.* **126** (3), 034502.

COLOMBET, D., LEGENDRE, D., COCKX, A., GUIRAUD, P., RISSO, F., DANIEL, C. & GALINAT, S. 2011 Experimental study of mass transfer in a dense bubble swarm. *Chem. Engng Sci.* **66** (14), 3432–3440.

COLOMBET, D., LEGENDRE, D., TUTTLIES, U., COCKX, A., GUIRAUD, P., NIEKEN, U., GALINAT, S. & DANIEL, C. 2018 On single bubble mass transfer in a volatile liquid. *Intl J. Heat Mass Transfer* **125**, 1144–1155.

CRIALESI-ESPOSITO, M., CHIBBARO, S. & BRANDT, L. 2023 The interaction of droplet dynamics and turbulence cascade. *Commun. Phys.* **6** (1), 5.

DEANE, G.B. & STOKES, M.D. 2002 Scale dependence of bubble creation mechanisms in breaking waves. *Nature* **418** (6900), 839.

DECKWER, W.-D. 1980 On the mechanism of heat transfer in bubble column reactors. *Chem. Engng Sci.* **35** (6), 1341–1346.

DEIKE, L. 2022 Mass transfer at the ocean–atmosphere interface: the role of wave breaking, droplets, and bubbles. *Annu. Rev. Fluid Mech.* **54**, 191–224.

DEIKE, L., MELVILLE, W.K. & POPINET, S. 2016 Air entrainment and bubble statistics in breaking waves. *J. Fluid Mech.* **801**, 91–129.

DI GIORGIO, S., PIROZZOLI, S. & IAFRATI, A. 2022 On coherent vortical structures in wave breaking. *J. Fluid Mech.* **947**, A44.

DODD, M.S., MOHADDES, D., FERRANTE, A. & IHME, M. 2021 Analysis of droplet evaporation in isotropic turbulence through droplet-resolved dns. *Intl J. Heat Mass Transfer* **172**, 121157.

DUGUID, H.A. & STAMPFER, J.F. JR. 1971 The evaporation rates of small, freely falling water drops. *J. Atmos. Sci.* **28** (7), 1233–1243.

FARSOIYA, P.K., MAGDELAINE, Q., ANTKOWIAK, A., POPINET, S. & DEIKE, L. 2023 Direct numerical simulations of bubble-mediated gas transfer and dissolution in quiescent and turbulent flows. *J. Fluid Mech.* **954**, A29.

FARSOIYA, P.K., POPINET, S. & DEIKE, L. 2021 Bubble-mediated transfer of dilute gas in turbulence. *J. Fluid Mech.* **920**, A34.

FIGUEROA-ESPINOZA, B. & LEGENDRE, D. 2010 Mass or heat transfer from spheroidal gas bubbles rising through a stationary liquid. *Chem. Engng Sci.* **65** (23), 6296–6309.

FRÖSSLING, N. 1938 Über die verdunstung fallender tropfen. *Gerlands Beitr. Geophys.* **52** (1), 170–216.

GAO, X., CHEN, J., QIU, Y., DING, Y. & XIE, J. 2022 Effect of phase change on jet atomization: a direct numerical simulation study. *J. Fluid Mech.* **935**, A16.

GARRETT, C., LI, M. & FARMER, D. 2000 The connection between bubble size spectra and energy dissipation rates in the upper ocean. *J. Phys. Oceanogr.* **30** (9), 2163–2171.

GAUDING, M., THIESSET, F., VAREA, E. & DANAILA, L. 2022 Structure of iso-scalar sets. *J. Fluid Mech.* **942**, A14.

GOROKHOVSKI, M. & HERRMANN, M. 2008 Modeling primary atomization. *Annu. Rev. Fluid Mech.* **40**, 343–366.

GUEYFFIER, D., LI, J., NADIM, A., SCARDOVELLI, R. & ZALESKI, S. 1999 Volume-of-fluid interface tracking with smoothed surface stress methods for three-dimensional flows. *J. Comput. Phys.* **152** (2), 423–456.

GVOZDIĆ, B., ALMÉRAS, E., MATHAI, V., ZHU, X., VAN GILS, D.P.M., VERZICCO, R., HUISMAN, S.G., SUN, C. & LOHSE, D. 2018 Experimental investigation of heat transport in homogeneous bubbly flow. *J. Fluid Mech.* **845**, 226–244.

HERLINA, H. & WISSINK, J.G. 2014 Direct numerical simulation of turbulent scalar transport across a flat surface. *J. Fluid Mech.* **744**, 217–249.

HERLINA, H. & WISSINK, J.G. 2016 Isotropic-turbulence-induced mass transfer across a severely contaminated water surface. *J. Fluid Mech.* **797**, 665–682.

HIDMAN, N., STRÖM, H., SASIC, S. & SARDINA, G. 2023 Assessing passive scalar dynamics in bubble-induced turbulence using direct numerical simulations. *J. Fluid Mech.* **962**, A32.

HIGBIE, R. 1935 The rate of absorption of a pure gas into a still liquid during short periods of exposure. *Trans. AIChE* **31**, 365–389.

HINZE, J.O. 1955 Fundamentals of the hydrodynamic mechanism of splitting in dispersion processes. *AIChE J.* **1** (3), 289–295.

HIROMITSU, N. & KAWAGUCHI, O. 1995 Influence of flow turbulence on the evaporation rate of a suspended droplet in a hot air flow. *Heat Transfer Japan Res.* **24** (8), 689–700.

JACQMIN, D. 1999 Calculation of two-phase Navier–Stokes flows using phase-field modelling. *J. Comput. Phys.* **155** (1), 96–127.

KASAGI, N., TOMITA, Y. & KURODA, A. 1992 Direct numerical simulation of passive scalar field in a turbulent channel flow. *J. Heat Transfer* **114** (3), 598–606.

KIM, J. & MOIN, P. 1989 Transport of passive scalars in a turbulent channel flow. In *Turbulent Shear Flows 6: Selected Papers from the Sixth International Symposium on Turbulent Shear Flows, Université Paul Sabatier, Toulouse, France, September 7–9, 1987*, pp. 85–96. Springer.

KIM, J., MOIN, P. & MOSER, R. 1987 Turbulence statistics in fully developed channel flow at low Reynolds number. *J. Fluid Mech.* **177**, 133.

KOLMOGOROV, A.N. 1941 The local structure of turbulence in incompressible viscous fluid for very large Reynolds number. *Dokl. Akad. Nauk SSSR* **30**, 9–13.

KORTEWEG, D.J. 1901 Sur la forme que prennent les equations du mouvements des fluides si l'on tient compte des forces capillaires causées par des variations de densité considérables mais continues et sur la théorie de la capillarité dans l'hypothèse d'une variation continue de la densité. *Arch. Néerland. Sci. Exact. Naturelles* **6**, 1–24.

KRISHNAMURTHY, D. & SUBRAMANIAN, G. 2018 Heat or mass transport from drops in shearing flows. Part 1. The open-streamline regime. *J. Fluid Mech.* **850**, 439–483.

KUERTEN, J.G. 2016 Point-particle DNS and LES of particle-laden turbulent flow-a state-of-the-art review. *Flow Turbul. Combust.* **97**, 689–713.

KWAKKEL, M., FERNANDINO, M. & DORAO, C.A. 2020 A redefined energy functional to prevent mass loss in phase-field methods. *AIP Adv.* **10** (6), 065124.

LAFAURIE, B., NARDONE, C., SCARDOVELLI, R., ZALESKI, S. & ZANETTI, G. 1994 Modelling merging and fragmentation in multiphase flows with SURFER. *J. Comput. Phys.* **113** (1), 134–147.

LEE, M. & MOSER, R.D. 2015 Direct numerical simulation of turbulent channel flow up to $Re_\tau \approx 5200$. *J. Fluid Mech.* **774**, 395–415.

LEVICH, V.G. 1962 *Physicochemical Hydrodynamics*. Prentice-Hall.

LI, Y., CHOI, J. & KIM, J. 2016 A phase-field fluid modeling and computation with interfacial profile correction term. *Commun. Nonlinear Sci.* **30** (1–3), 84–100.

LIU, H.-R., CHONG, K.L., YANG, R., VERZICCO, R. & LOHSE, D. 2022 Heat transfer in turbulent Rayleigh–Bénard convection through two immiscible fluid layers. *J. Fluid Mech.* **938**, A31.

LU, J. & TRYGGVASON, G. 2007 Effect of bubble size in turbulent bubbly downflow in a vertical channel. *Chem. Engng Sci.* **62**, 3008–3018.

MAGAR, V. & PEDLEY, T.J. 2005 Average nutrient uptake by a self-propelled unsteady squirmer. *J. Fluid Mech.* **539**, 93–112.

MAGNAUDET, J. & EAMES, I. 2000 The motion of high-Reynolds-number bubbles in inhomogeneous flows. *Annu. Rev. Fluid Mech.* **32** (1), 659–708.

MANGANI, F., SOLIGO, G., ROCCON, A. & SOLDATI, A. 2022 Influence of density and viscosity on deformation, breakage, and coalescence of bubbles in turbulence. *Phys. Rev. Fluids* **7** (5), 053601.

MARTI, F., MARTINEZ, O., MAZO, D., GARMAN, J. & DUNN-RANKIN, D. 2017 Evaporation of a droplet larger than the Kolmogorov length scale immersed in a relative mean flow. *Intl J. Multiphase Flow* **88**, 63–68.

MARTIN, M.J. & BOYD, I.D. 2006 Momentum and heat transfer in a laminar boundary layer with slip flow. *J. Thermophys. Heat Transfer* **20** (4), 710–719.

MAXEY, M. 2017 Simulation methods for particulate flows and concentrated suspensions. *Annu. Rev. Fluid Mech.* **49**, 171–193.

MÉÈS, L., GROSJEAN, N., MARIÉ, J.-L. & FOURNIER, C. 2020 Statistical Lagrangian evaporation rate of droplets released in a homogeneous quasi-isotropic turbulence. *Phys. Rev. Fluids* **5** (11), 113602.

MICHAELIDES, E.E. 2003 Hydrodynamic force and heat/mass transfer from particles, bubbles, and drops–the Freeman scholar lecture. *J. Fluids Engng* **125** (2), 209–238.

MIRJALILI, S., JAIN, S.S. & MANI, A. 2022 A computational model for interfacial heat and mass transfer in two-phase flows using a phase field method. *Intl J. Heat Mass Transfer* **197**, 123326.

MIRJALILI, S., KHANWALE, M.A. & MANI, A. 2023 Assessment of an energy-based surface tension model for simulation of two-phase flows using second-order phase field methods. *J. Comput. Phys.* **474**, 111795.

MIRJALILI, S. & MANI, A. 2021 Consistent, energy-conserving momentum transport for simulations of two-phase flows using the phase field equations. *J. Comput. Phys.* **426**, 109918.

NI, R. 2024 Deformation and breakup of bubbles and drops in turbulence. *Annu. Rev. Fluid Mech.* **56**, 2024.

OHTA, Y., SHIMOYAMA, K. & OHIGASHI, S. 1975 Vaporization and combustion of single liquid fuel droplets in a turbulent environment. *Bull. JSME* **18** (115), 47–56.

PELUSI, F., ASCIONE, S., SBRAGAGLIA, M. & BERNASCHI, M. 2023 Analysis of the heat transfer fluctuations in the Rayleigh-Bénard convection of concentrated emulsions with finite-size droplets. *Soft Matt.* **19**, 7192–7201.

PERLEKAR, P., BIFERALE, L. & SBRAGAGLIA, M. 2012 Droplet size distribution in homogeneous isotropic turbulence. *Phys. Fluids* **065101**, 1–10.

PIROZZOLI, S., BERNARDINI, M. & ORLANDI, P. 2016 Passive scalars in turbulent channel flow at high Reynolds number. *J. Fluid Mech.* **788**, 614–639.

PIROZZOLI, S., ROMERO, J., FATICA, M., VERZICCO, R. & ORLANDI, P. 2021 One-point statistics for turbulent pipe flow up to. *J. Fluid Mech.* **926**, A28.

PRANDTL, L. 1905 Uber flussigkeitsbewegung bei sehr kleiner reibung. In *Verhandlungen des III. Internationalen Mathematiker Kongresses, Heidelberg (1904), Leipzig*. pp. 485–491. B.G. Teubner.

QI, Y., TAN, S., CORBITT, N., URBANIK, C., SALIBINDLA, A.K.R. & NI, R. 2022 Fragmentation in turbulence by small eddies. *Nat. Commun.* **13** (1), 469.

RANZ, W.E. 1952 Evaporation from drops-I and-II. *Chem. Engng Prog.* **48**, 141–146.

ROCCON, A., DE PAOLI, M., ZONTA, F. & SOLDATI, A. 2017 Viscosity-modulated breakup and coalescence of large drops in bounded turbulence. *Phys. Rev. Fluids* **2**, 083603.

ROCCON, A., ZONTA, F. & SOLDATI, A. 2023 Phase-field modeling of complex interface dynamics in drop-laden turbulence. *Phys. Rev. Fluids* **8**, 090501.

SCAPIN, N., DALLA BARBA, F., LUPO, G., ROSTI, M.E., DUWIG, C. & BRANDT, L. 2022 Finite-size evaporating droplets in weakly compressible homogeneous shear turbulence. *J. Fluid Mech.* **934**, A15.

SCARBOLO, L., BIANCO, F. & SOLDATI, A. 2016 Turbulence modification by dispersion of large deformable droplets. *Eur. J. Mech. (B/Fluids)* **55**, 294–299.

SCARBOLO, L. & SOLDATI, A. 2013 Turbulence modulation across the interface of a large deformable drop. *J. Turbul.* **14**, 27–43.

SCHLICHTING, H. & GERSTEN, K. 2016 *Boundary-Layer Theory*. Springer.

SHAO, C., JIN, T. & LUO, K. 2022 The interaction between droplet evaporation and turbulence with interface-resolved direct numerical simulation. *Phys. Fluids* **34** (7), 072102.

SOLIGO, G., ROCCON, A. & SOLDATI, A. 2019*a* Breakage, coalescence and size distribution of surfactant-laden droplets in turbulent flow. *J. Fluid Mech.* **881**, 244–282.

SOLIGO, G., ROCCON, A. & SOLDATI, A. 2019*b* Coalescence of surfactant-laden drops by phase field method. *J. Comput. Phys.* **376**, 1292–1311.

SOLIGO, G., ROCCON, A. & SOLDATI, A. 2019*c* Mass conservation improved phase field methods for turbulent multiphase flow simulation. *Acta Mech.* **230**, 683–696.

SOLIGO, G., ROCCON, A. & SOLDATI, A. 2020 Effect of surfactant-laden droplets on turbulent flow topology. *Phys. Rev. Fluids* **5** (7), 073606.

SOLIGO, G., ROCCON, A. & SOLDATI, A. 2021 Turbulent flows with drops and bubbles: what numerical simulations can tell us – Freeman scholar lecture. *Trans. ASME J. Fluids Engng* **143**, 080801–1.

SPEZIALE, C.G. 1987 On the advantages of the vorticity-velocity formulation of the equations of fluid dynamics. *J. Comput. Phys.* **73** (2), 476–480.

THAN, P., PREZIOSI, L., JOSEPH, D.D. & ARNEY, M. 1988 Measurement of interfacial tension between immiscible liquids with the spinning road tensiometer. *J. Colloid Interface Sci.* **124** (2), 552–559.

THEOFANOUS, T.G., HOUZE, R.N. & BRUMFIELD, L.K. 1976 Turbulent mass transfer at free, gas-liquid interfaces, with applications to open-channel, bubble and jet flows. *Intl J. Heat Mass Transfer* **19** (6), 613–624.

VELA-MARTÍN, A. & AVILA, M. 2022 Memoryless drop breakup in turbulence. *Sci. Adv.* **8** (50), eabp9561.

WANG, J., ALIPOUR, M., SOLIGO, G., ROCCON, A., DE PAOLI, M., PICANO, F. & SOLDATI, A. 2021*a* Short-range exposure to airborne virus transmission and current guidelines. *Proc. Natl Acad. Sci. USA* **118** (37), e2105279118.

WANG, J., DALLA BARBA, F. & PICANO, F. 2021*b* Direct numerical simulation of an evaporating turbulent diluted jet-spray at moderate Reynolds number. *Intl J. Multiphase Flow* **137**, 103567.

WANNINKHOF, R. 1992 Relationship between wind speed and gas exchange over the ocean. *J. Geophys. Res.* **97** (C5), 7373–7382.

WHITAKER, S. 1972 Forced convection heat transfer correlations for flow in pipes, past flat plates, single cylinders, single spheres, and for flow in packed beds and tube bundles. *AIChE J.* **18** (2), 361–371.

WU, J.-S., HSU, K.-H., KUO, P.-M. & SHEEN, H.-J. 2003 Evaporation model of a single hydrocarbon fuel droplet due to ambient turbulence at intermediate Reynolds numbers. *Intl J. Heat Mass Transfer* **46** (24), 4741–4745.

YUE, P., ZHOU, C. & FENG, J.J. 2007 Spontaneous shrinkage of drops and mass conservation in phase-field simulations. *J. Comput. Phys.* **223** (1), 1–9.

ZHENG, X., BABAEE, H., DONG, S., CHRYSSOSTOMIDIS, C. & KARNIADAKIS, G.E. 2015 A phase-field method for 3D simulation of two-phase heat transfer. *Intl J. Heat Mass Transfer* **82**, 282–298.

ZONTA, F., MARCHIOLI, C. & SOLDATI, A. 2012*a* Modulation of turbulence in forced convection by temperature-dependent viscosity. *J. Fluid Mech.* **697**, 150–174.

ZONTA, F., ONORATO, M. & SOLDATI, A. 2012*b* Turbulence and internal waves in stably-stratified channel flow with temperature-dependent fluid properties. *J. Fluid Mech.* **697**, 175–203.

ZONTA, F. & SOLDATI, A. 2014 Effect of temperature-dependent fluid properties on heat transfer in turbulent mixed convection. *Trans. ASME J. Heat Transfer* **136**, 022501.